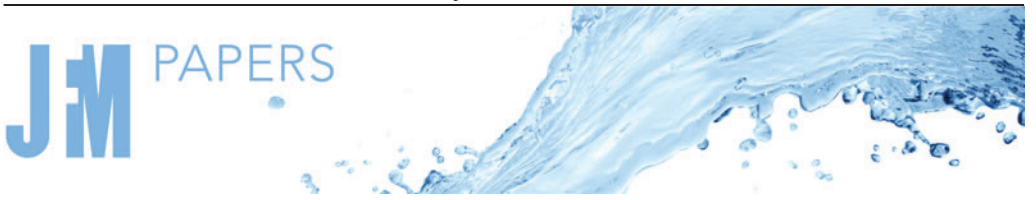
J. Fluid Mech. (2022), *vol*. 941, A14, doi:10.1017/jfm.2022.285



Analysis of interscale energy transfer in a boundary layer undergoing bypass transition

H. Yao[1], J.-P. Mollicone[2] and G. Papadakis[1],†

[1]Department of Aeronautics, Imperial College London, London SW7 2AZ, UK

[2]Department of Mechanical Engineering, Faculty of Engineering, University of Malta, Msida MSD 2080, Malta

(Received 13 May 2021; revised 20 January 2022; accepted 29 March 2022)

The Kármán–Howarth–Monin–Hill equation is employed to study the production and interscale energy transfer in a boundary layer undergoing bypass transition due to free-stream turbulence. The energy flux between different length scales is calculated at several streamwise locations covering the laminar, transitional and turbulent regimes. Maps of scale energy production and flux vectors are visualised on two-dimensional planes and three-dimensional hyper-planes that comprise both physical and separation spaces. In the transitional region, the maps show strong inverse cascade in the streamwise direction near the wall. The energy flux vectors emanate from a region of strong production and transfer energy to larger streamwise scales. To provide deeper insight into the origin of the inverse cascade process, we decompose the energy flux vector into components arising from nonlinear interactions between velocity fluctuations, mean flow inhomogeneity, pressure and viscous effects. The inverse cascade is mainly due to the nonlinear interaction component, and in the earliest stages of transition this component competes with that due to mean flow inhomogeneity. By superposing the instantaneous velocity fields and the energy flux vectors, we relate the inverse cascade process to the growth of turbulent spots. Once the transition process is complete, the maps become very similar to those observed in other fully developed turbulent flows, such as channel flow. Finally we characterise the nonlinear interaction term using probability density functions (PDFs) evaluated at different wall-normal heights. The PDFs are asymmetric and wide-skirted as in homogeneous isotropic turbulence, but are skewed towards positive values reflecting the inverse cascade.

Key words: turbulent boundary layers, turbulent transition, transition to turbulence

† Email address for correspondence: g.papadakis@ic.ac.uk

© The Author(s), 2022. Published by Cambridge University Press

https://doi.org/10.1017/jfm.2022.285 Published online by Cambridge University Press

1. Introduction

The process of transition from laminar to turbulent flow that does not arise from exponentially growing Tollmien–Schliching instabilities is referred to as bypass transition (Morkovin 1969). Bypass transition comprises three main phases: streak formation and growth in the laminar region, secondary instability of streaks that leads to intermittent formation of turbulent spots and finally spot growth and merging that eventually leads to a fully turbulent flow. In the present paper we study a boundary layer undergoing bypass transition due to free-stream turbulence; this occurs in many engineering applications that operate in a high-disturbance environment, such as turbomachinery flows.

In the laminar region, the shear sheltering mechanism (Hunt & Durbin 1999; Zaki & Saha 2009) filters the high-frequency velocity components and allows only low-frequency modes to penetrate inside the boundary layer. These interact with mean shear producing high- and low-speed streaky structures, known as Klebanoff modes (Klebanoff 1971; Kendall 1991). Different views on the formation of these structures are summarised in Durbin (2017). The inflectional velocity profile along the spanwise direction arising from the low- and high-speed streaks triggers secondary instabilities and leads to breakdown into turbulent spots (Andersson *et al.* 2001; Vaughan & Zaki 2011).

The appearance and growth of turbulent patches (spots) in a transitional boundary layer was first documented in the experimental work of Emmons (1951). Since then numerous experimental and numerical investigations have focused on the characterisation of artificially or spontaneously generated spots (e.g. (Wygnanski, Sokolov & Friedman 1976; Cantwell, Coles & Dimotakis 1978; Perry, Lim & Teh 1981; Singer 1996; Anthony, Jones & Lagraff 2005; Park *et al.* 2012; Nolan & Zaki 2013; Wu *et al.* 2017; Marxen & Zaki 2019; Wang *et al.* 2021)). These studies have investigated the three-dimensional spot shape, growth, propagation speeds of leading and trailing edges, as well as other finer structural details. Although there are differences between artificially generated spots (for example due to wall actuation) and those appearing intermittently in a streaky boundary layer undergoing bypass transition (Jacobs & Durbin 2001; Anthony *et al.* 2005), all the above studies agree that once spots form, they grow in size and coalesce, leading eventually to a fully developed turbulent boundary layer.

Intuitively, this process of growth of a nascent turbulent patch to a larger one, and the subsequent merging of nearby patches, is reminiscent of an inverse energy cascade process, in which energy flows from small to large scales. For example, in two-dimensional turbulence, the inverse energy cascade results in the growth of the integral length scale (chapter 10 in Davidson 2015). There are several questions around this notion that have not been considered so far in the literature: what it the mechanism that causes the growth of spots, especially in the streamwise direction? Is this indeed related to inverse energy cascade? How can this process be characterised quantitatively? More generally, how does energy transfer between different length scales in transitional flows differ from that in fully developed turbulent flows? The central aim of the paper is to shed more light onto these questions.

The standard approach to describe the dynamics of energy transfer is the turbulent kinetic energy (TKE) equation. This equation governs the evolution of TKE in physical space and contains the mechanisms that determine this evolution, such as production, dissipation, advection by the mean flow and fluctuations, etc. However, this is a single-point equation, and does not contain information about the energy of different length scales, therefore not being suitable for answering the above questions. On the other hand, if the flow is homogeneous in all directions, one can employ Fourier series and derive an evolution equation for the energy spectrum $E(k)$ (see Pope 2000; Davidson 2015).

https://doi.org/10.1017/jfm.2022.285 Published online by Cambridge University Press

This equation, formulated in spectral space, contains a term representing the kinetic energy transfer between scales (characterised by wavenumbers). It is also possible to formulate the problem in real space (see Davidson 2015; Davidson & Pearson 2005). The equivalence between the two formulations arises from the fact that one can identify distributions of TKE among eddies defined in either real or Fourier space. For example, a random distribution and orientation of Townsend eddies with characteristic length scale ℓ_e results in a continuous spectrum $E(k)$ that peaks at $k \approx \pi/\ell_e$ (for details, see Townsend (1976) and Davidson (2015)). Thus eddies of a single size contribute to $E(k)$ across the whole range of wavenumbers, but there is a distinct peak.

For inhomogeneous flows, we can formulate the problem only in real space using the generalised Kármán–Howarth equation. This is a balance equation for the second-order structure function and is formulated in a six-dimensional space, which comprises both the physical and scale spaces. The second-order structure function is defined locally at a point X_i in physical space, using the square of the difference between the fluctuating velocities at two points, $x_i^+ = X_i + \frac{1}{2}r_i$ and $x_i^- = X_i - \frac{1}{2}r_i$. This can be thought of as the energy of eddies with size smaller than $r = |r_i|$; refer to Davidson (2015) for more details (and the caveats of this interpretation for eddies with size much smaller than r and close to dissipation scales).

The equation was first derived for homogeneous isotropic turbulence by de Kármán & Howarth (1938) using the two-point velocity correlation tensor. Later Kolmogorov (1941) reformulated the equation in terms of structure functions and proved the famous $-4/5$ law that links the interscale energy flux, the separation between the two points and the dissipation rate. Under homogeneous isotropic turbulence conditions, this flux is always negative, indicating forward cascade, i.e. energy is transferred from large to small scales. The advantage of this equation is that even for homogeneous isotropic turbulence, it is expressed in spatial variables, rather than wavenumbers. This feature allows for generalisation to more complex flows, which includes the effect of anisotropy, shear and convection due to mean flow (Monin & Yaglom 1975; Antonia *et al.* 1997, 2000; Danaila *et al.* 2001, 2012; Danaila, Anselmet & Zhou 2004).

The most general form of the equation appears in Hill (2002). For a weak formulation, which is more suitable for non-smooth, i.e. rough, velocity fields, see Duchon & Robert (2000) and Dubrulle (2019). The equation is derived directly from the Navier–Stokes equation applied at points x_i^+ and x_i^- and contains all the mechanisms that determine the evolution of the second-order structure function, i.e. how the energy at a particular scale is affected by production, dissipation and transfer in the physical X_i and scale r_i spaces. It does not make the assumptions of homogeneity and/or isotropy, and is thus suitable for our purposes. We note that in the limit of very large separations r, the Kármán–Howarth–Monin–Hill (KHMH) equation tends to the TKE (more precisely, it tends to twice the sum of the TKEs at points x_i^+ and x_i^-; see more details in § 3).

This equation has been applied extensively to fully developed, wall-bounded turbulent flows. It was employed for the first time by Marati, Casciola & Piva (2004) to a low-Reynolds-number channel flow. The results showed that the well-known zonal decomposition of the flow in viscous layer, buffer region, logarithmic layer and bulk region is also meaningful in the context of a scale-by-scale budget. Saikrishnan *et al.* (2012) studied the effect of Reynolds number in the range $Re_\tau = 180$–934 on the scale energy balance, while Cimarelli & De Angelis (2012) focused on $Re_\tau = 300$ and investigated in particular the inverse cascade for length scales larger than a cut-off value, and the associated difficulties for large-eddy simulation subgrid-scale modelling if the filter size is larger than this value. Visualisation of the scale energy flux in a three-dimensional

https://doi.org/10.1017/jfm.2022.285 Published online by Cambridge University Press

hyper-plane (Cimarelli, De Angelis & Casciola 2013) revealed spiral-like paths that originate from two energy sources, one located close to the wall (inner region) and the other further away (outer region). In Cimarelli *et al.* (2015) particular attention was paid to the dynamics of the outer source, while in Cimarelli *et al.* (2016) the role of attached eddies on sustaining a reverse cascade towards the bulk flow was studied. More recently, Gatti *et al.* (2020) considered the balance equations for all components of the second-order structure function tensor and the interactions via the pressure-strain term.

The preceding short review has focused on attached wall-bounded flows as more relevant to the subject of this paper, but the equation has been applied to several other inhomogeneous and anisotropic flows, such as the near wake behind a square prism (Alves Portela, Papadakis & Vassilicos 2017, 2020), von Kármán flows (Dubrulle 2019; Knutsen *et al.* 2020), planar jets (Cimarelli *et al.* 2021) and the recirculating flow behind a bump (Mollicone *et al.* 2018).

The success of the KHMH equation in describing the complex interscale dynamics of near-wall turbulence justifies the adoption of this framework to explore similar issues in bypass transition. As explained earlier, the equation is very general, and therefore applicable in laminar, transitional and fully turbulent regimes. Thus, it can be employed across the laminar–turbulent interface, allowing us to get a unique glimpse of the interscale energy transfer process in transitional flows.

The paper is organised as follows. In § 2 the flow conditions for the case considered are briefly described and comparisons against reference data from the literature are presented. In § 3 we introduce the KHMH equation, while in §§ 4 to 7 scale energy fluxes in two-dimensional planes and three-dimensional hyper-planes are presented and discussed. In § 8 we relate the observed fluxes with the instantaneous flow fields (that contain laminar regions and turbulent patches) and investigate their probability density functions (PDFs). We conclude in § 9.

2. Test case details and one-point statistics

We consider the transitional flow in a flat-plate boundary layer. The turbulence intensity in the free stream is set to 3.4 %, and the fluctuations are assumed to follow a von Kármán spectrum. Spatial coordinates are normalised by the Blasius similarity variable $L_0 = \sqrt{\nu X_0/U_\infty}$, where X_0 is the distance of the domain inlet from the leading edge of the plate, U_∞ is the free-stream velocity and ν the kinematic viscosity of the fluid. The integral length scale of free-stream turbulence is set to $L_{11} = 5L_0$, which is approximately equal to the boundary layer thickness at the inlet. The Reynolds number based on the Blasius similarity variable is $Re_{L_0} = 160$ (or $Re_\theta = 110$ based on momentum thickness). The computational domain in the streamwise (X), wall-normal (Y) and spanwise (Z) directions is $3000 \times 200 \times 150$. This domain is discretised using $2049 \times 192 \times 169$ cells in the X, Y and Z directions, respectively. The grid spacings in wall units are $\Delta x^+_{max} \approx 11.78$, $\Delta y^{+(w)}_{max} \approx 0.24$ and $\Delta z^+_{max} \approx 7.14$. The subscript *max* denotes maximum values in the fully turbulent region, while $\Delta y^{+(w)}_{max}$ is evaluated at the centroid of the first cell close to the wall.

We employ a previously generated direct numerical simulation database for the aforementioned conditions; refer to Yao, Alves-Portela & Papadakis (2020) for details regarding generation of inlet conditions, numerical schemes in space and time, order of accuracy, Courant–Friedrichs–Lewy numbers, etc. The database comprises 350 instantaneous snapshots of the flow. The time separation between two snapshots is $20T_0$,

https://doi.org/10.1017/jfm.2022.285 Published online by Cambridge University Press

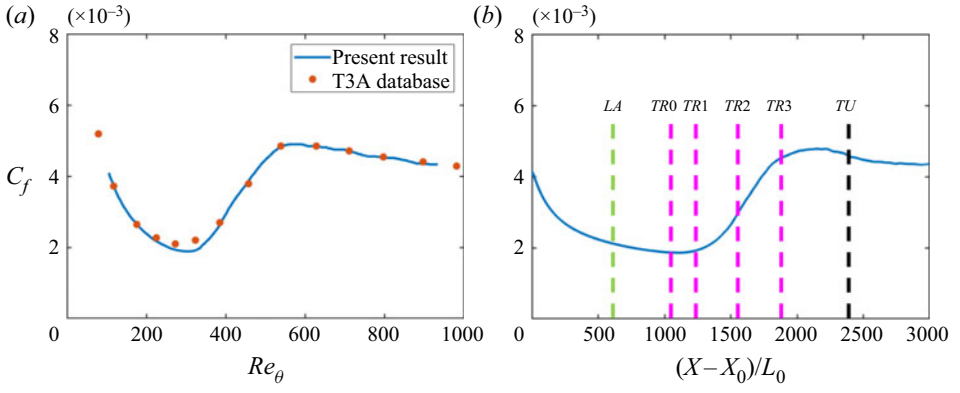


Figure 1. Skin friction coefficient C_f against Re_θ (*a*) and distance from the inlet of the domain $(X - X_0)/L_0$ (*b*). The green and black vertical lines denote locations at the laminar (*LA*) and turbulent (*TU*) regions, respectively. The purple vertical lines denote four stations *TR*0, *TR*1, *TR*2, *TR*3 within the transitional region. The coordinates are $(X - X_0)/L_0 = 540$, 1065, 1215, 1515, 1815 and 2415 for *LA*, *TR*0, *TR*1, *TR*2, *TR*3 and *TU*, respectively.

where $T_0 = L_0/U_\infty$. To increase the number of samples and improve convergence of the statistics, we perform both time and spanwise averaging.

Figure 1 shows the variation of the friction coefficient C_f as the flow transitions from laminar to turbulent. The results match well with the experiments of the T3A database (Roach 1990). Note that in the experiment, the free-stream turbulence intensity is set to 3.3 %; however, in the current simulation, 3.4 % is used (as already mentioned) in order to match the transition onset. We study the spatial evolution of the interscale energy fluxes at six locations, placed in the laminar (*LA*), transitional (*TR*0, *TR*1, *TR*2, *TR*3) and fully turbulent (*TA*) regions; these locations are shown in figure 1(*b*).

Before we proceed to examine the evolution of two-point statistics using the KHMH equation, it is instructive to examine first the budgets of the TKE equation,

$$\underbrace{\frac{\partial (U_i k)}{\partial x_i}}_{\text{convection}(\mathcal{A}_k)} = \underbrace{-\langle u_i u_j \rangle \frac{\partial U_j}{\partial x_i}}_{\text{production}(\mathcal{P}_k)} \underbrace{- \nu \left\langle \frac{\partial u_j}{\partial x_i} \frac{\partial u_j}{\partial x_i} \right\rangle}_{\text{dissipation}(\epsilon_k)} + \underbrace{\frac{\partial}{\partial x_i}\left(\nu \frac{\partial k}{\partial x_i}\right)}_{\text{viscous diffusion}(\mathcal{D}_k)} \underbrace{- \frac{\partial}{\partial x_i}\left(\frac{1}{2}\langle u_i u_j u_j \rangle\right)}_{\text{turbulent diffusion}(\mathcal{T}_k)} \underbrace{- \frac{\partial}{\partial x_i}\left(\frac{1}{\rho}\langle u_i p \rangle\right)}_{\text{pressure diffusion}(\mathcal{T}_{p,k})}, \tag{2.1}$$

at these six locations. Figure 2 shows the evolution of the budget terms plotted against the distance from the wall for all streamwise positions; variables are normalised using the local wall units. The open symbols represent the reference direct numerical simulation data of Spalart (1988) and are repeated in every panel. The matching between the present results at the *TU* region (where $Re_\theta = 800$) and the reference data (where $Re_\theta = 1410$) is very good for all terms. This provides further evidence of the validity of the generated database. Comparison between the lines and symbols indicates the deviation from the fully turbulent state at each location.

In the laminar regime (figure 2*a*), where the boundary layer is distorted by Klebanoff modes, the production term has an approximately symmetric shape, peaks at $Y^+ \approx 21$ and reaches a relatively small value. As the flow transitions, the production peak grows,

https://doi.org/10.1017/jfm.2022.285 Published online by Cambridge University Press

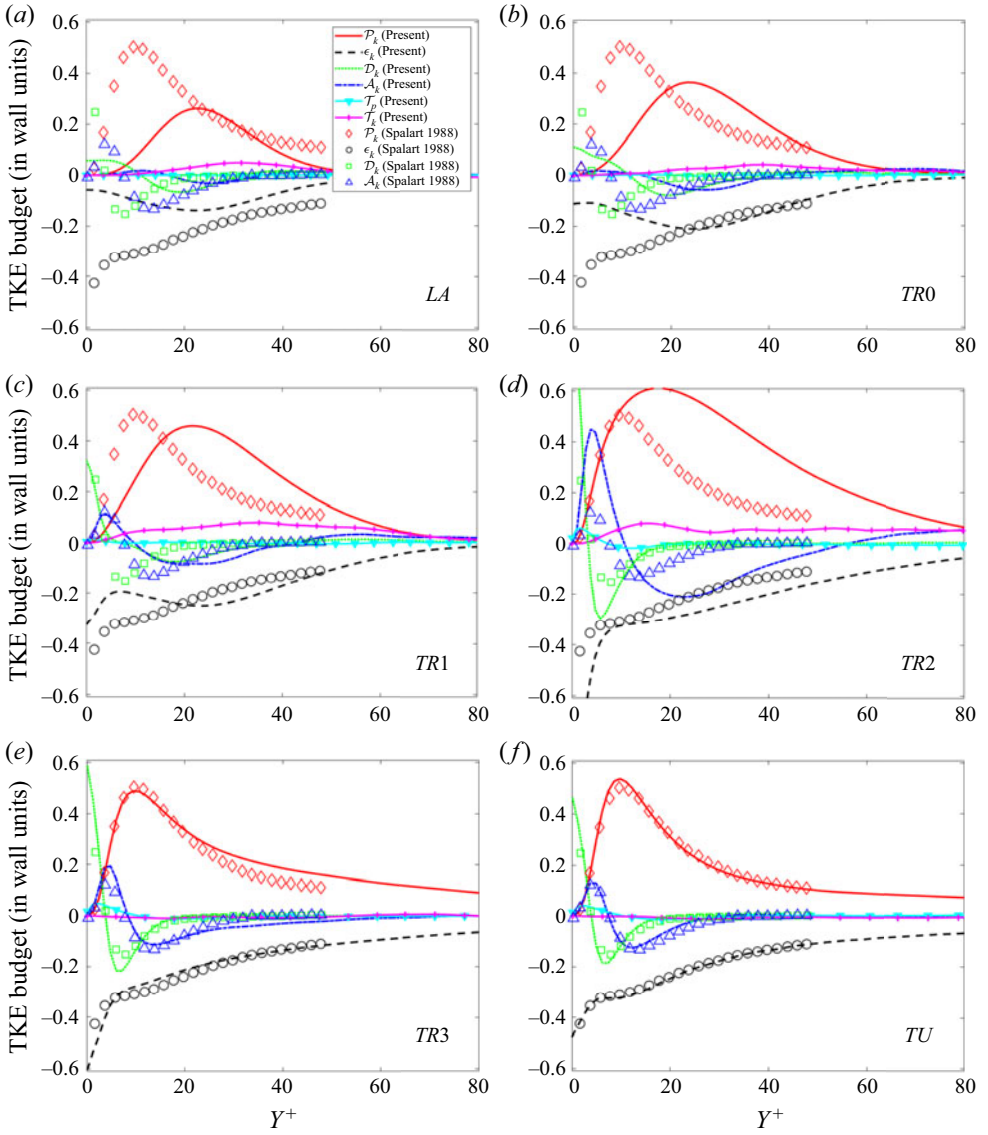


Figure 2. The TKE budgets at locations (*a*) *LA*, (*b*) *TR*0, (*c*) *TR*1, (*d*) *TR*2, (*e*) *TR*3 and (*f*) *TU*. The symbols represent data from Spalart (1988) for $Re_\theta = 1410$.

moves closer to the wall and finally settles at $Y^+ \approx 16$ (figure 2*f*), i.e. in the buffer layer. A production overshoot appears at *TR*2, which is in the middle of the transition region. At this position the maximum intermittency is about 40 % (refer to figure 4 of Yao *et al.* (2020)) and grows fast indicating the rapid formation and growth of turbulent spots. Nolan & Zaki (2013) report an overshoot in the streamwise root-mean-square velocity in exactly the same position, i.e. when the skin friction is midway between the laminar and turbulent values.

At *LA*, dissipation peaks within the Klebanoff mode core, but further downstream the maximum value grows, and beyond *TR*1 it settles at the wall, where it is balanced by viscous diffusion, as expected. Turbulent diffusion has small contribution at *LA*, *TR*0 and

https://doi.org/10.1017/jfm.2022.285 Published online by Cambridge University Press

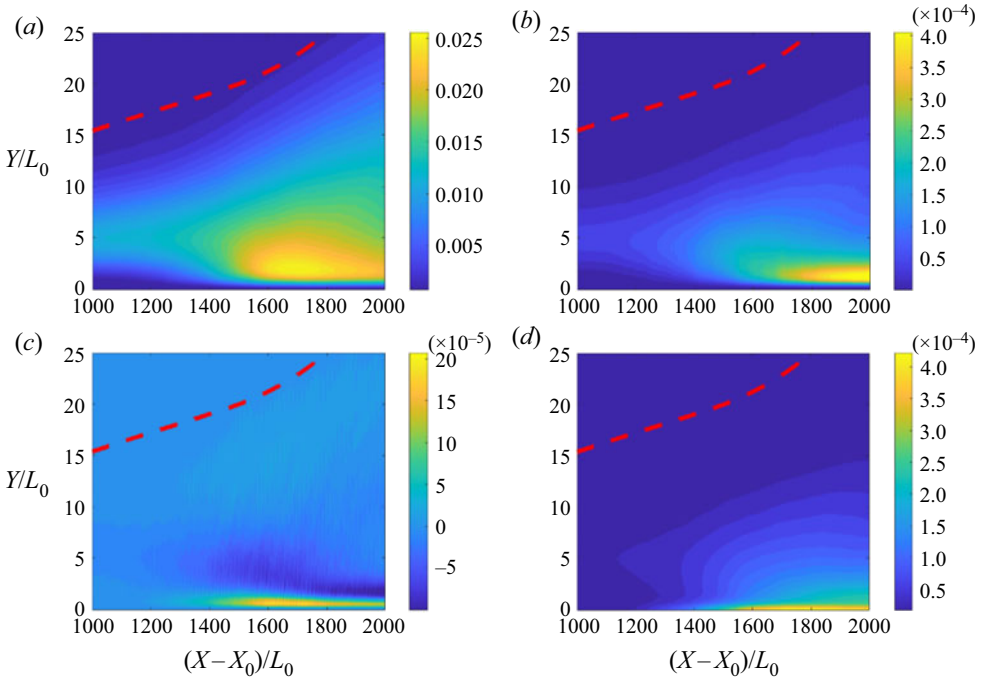


Figure 3. Contour plots of (*a*) TKE, (*b*) production, (*c*) turbulent diffusion and (*d*) dissipation. All variables are normalised with global units. The red dashed line indicates the location of the boundary layer thickness.

*TR*1, but becomes very significant at *TR*2, with a sharp positive peak close to the wall at $Y^+ \approx 5$ and a shallower negative trough at $Y^+ \approx 22$. At this location, three terms dominate for $Y^+ > 15$: production, dissipation and turbulent diffusion. Note also the very sharp rise of dissipation close to the wall, and the important contribution of turbulent diffusion to balance it. Further downstream, at *TR*3 and *TU*, all terms settle to smaller values.

The largest deviation from equilibrium, quantified by the difference between production and dissipation for $Y^+ > 15$, appears in *TR*2; this is the position with the largest growth of C_f as evidenced in figure 1, consistent with the rapid increase of intermittency, as mentioned earlier. At *TR*3, where C_f starts to stabilise marking the end of transition, the budgets are very similar to those at the fully turbulent state, *TU*. In the latter state turbulence is in equilibrium, with production balancing dissipation for $Y^+ > 25$. In all locations the convection term plays a minor role. It becomes more important in *TR*2 (and less so in *TR*1) for $Y^+ > 60$, where it balances production, dissipation and turbulent diffusion.

The strong wall-normal and streamwise inhomogeneity are more clearly demonstrated in the contour plots of TKE, production, turbulent transport and dissipation shown in figure 3, where all terms are normalised by global variables (free-stream velocity U_∞ and Blasius variable at the inlet L_0). Turbulent kinetic energy and turbulent transport peak at $(X - X_0)/L_0 \approx 1650$, slightly downstream of *TR*2. When normalised with global variables, the production term reaches maximum in the turbulent regime. The peak of TKE therefore at $(X - X_0)/L_0 \approx 1650$ arises from the strong positive value of turbulent transport close to the wall (yellow region in figure 3*c*). Dissipation grows sharply downstream of $(X - X_0)/L_0 \approx 1600$ and is maximised at the wall.

https://doi.org/10.1017/jfm.2022.285 Published online by Cambridge University Press

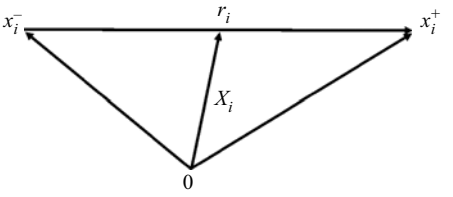


Figure 4. Schematic of the points x_i^+ and x_i^- used to define δq^2, the midpoint X_i and the separation vector r_i.

The TKE is a one-point equation and energy is transported only in physical space. In the next section we look at the transport of energy in both physical and scale spaces using the KHMH equation.

3. Two-point KHMH equation

The KHMH equation is a balance equation for the second-order structure function, defined as $\delta q^2 = (\delta u_i)^2 = (u_i^+ - u_i^-)^2$, where u_i^+ and u_i^- are the velocity fluctuations around the time averages U_i^+ and U_i^- at two points x_i^+ and x_i^-, respectively (refer to figure 4). Denoting the midpoint as $X_i = 0.5(x_i^+ + x_i^-)$ and the separation between the two points as $r_i = x_i^+ - x_i^-$, it is evident that for a general three-dimensional inhomogeneous and anisotropic flow, δq^2 is a function of three spatial and three separation (or scale) variables, i.e. $\delta q^2(X_i, r_i)$. Using angular brackets to represent time averages, the transport equation of $\langle \delta q^2(X_i, r_i)\rangle$ takes the form (Hill 2002)

$$\underbrace{\frac{\partial \langle \delta q^2\rangle}{\partial t}}_{\substack{\text{Transient}\\ \text{term } (\mathcal{A}_t)}} + \underbrace{\frac{\partial \dfrac{(U_i^+ + U_i^-)}{2}\langle \delta q^2\rangle}{\partial X_i}}_{\text{Mean flow advection}(\mathcal{A}_U)} + \underbrace{\frac{\partial \langle \delta u_i \delta q^2\rangle}{\partial r_i}}_{\substack{\text{Nonlinear interscale}\\ \text{transfer } (\Pi)}} + \underbrace{\frac{\partial \delta U_i \langle \delta q^2\rangle}{\partial r_i}}_{\substack{\text{Linear interscale}\\ \text{transfer } (\Pi_U)}}$$

$$= \underbrace{-\frac{\partial \left\langle \dfrac{(u_i^+ + u_i^-)}{2}\delta q^2 \right\rangle}{\partial X_i}}_{\substack{\text{Turbulent}\\ \text{advection } (\mathcal{A}_u)}} \underbrace{-2\frac{\partial \langle \delta u_i \delta p\rangle}{\partial X_i}}_{\substack{\text{Pressure-velocity}\\ \text{correlation } (\mathcal{T}_p)}} + \underbrace{\frac{1}{2}\nu \frac{\partial^2 \langle \delta q^2\rangle}{\partial X_i \partial X_i}}_{\substack{\text{Diffusion in physical}\\ \text{space } (\mathcal{D}_x)}}$$

$$+ \underbrace{2\nu \frac{\partial^2 \langle \delta q^2\rangle}{\partial r_i \partial r_i}}_{\substack{\text{Diffusion in scale}\\ \text{space } (\mathcal{D}_r)}} \underbrace{-2\langle \delta u_i \delta u_j\rangle \frac{\partial \delta U_j}{\partial r_i} - \langle (u_i^+ + u_i^-)\delta u_j\rangle \frac{\partial \delta U_j}{\partial X_i}}_{\text{Production by mean flow}(\mathcal{P})}$$

$$- \underbrace{4\nu \left(\frac{1}{4}\left\langle \frac{\partial \delta u_j}{\partial X_i}\frac{\partial \delta u_j}{\partial X_i}\right\rangle + \left\langle \frac{\partial \delta u_j}{\partial r_i}\frac{\partial \delta u_j}{\partial r_i}\right\rangle \right)}_{\text{Dissipation}(\epsilon)}. \tag{3.1}$$

As noted in the introduction, $\langle \delta q^2\rangle$ can be interpreted as the energy of eddies with size smaller than $r = |r_i|$. For statistically steady flows, as the ones considered in the present paper, the transient term $\mathcal{A}_t = 0$. Defining $U_i^* = (U_i^+ + U_i^-)/2$ and $u_i^* = (u_i^+ + u_i^-)/2$ as the midpoint values of the mean and fluctuating velocities, respectively, and grouping

https://doi.org/10.1017/jfm.2022.285 Published online by Cambridge University Press

together the terms computed in physical (X_i) and scale (r_i) spaces, (3.1) can be rearranged as

$$\underbrace{\frac{\partial\left[\langle U_i^*\delta q^2\rangle+\langle u_i^*\delta q^2\rangle+\langle 2\delta u_i\delta p\rangle-\frac{1}{2}\nu\frac{\partial\langle\delta q^2\rangle}{\partial x_i}\right]}{\partial X_i}}_{\text{Transport in physical space}}+\underbrace{\frac{\partial\left[\langle\delta u_i\delta q^2\rangle+\langle\delta U_i\delta q^2\rangle-2\nu\frac{\partial\langle\delta q^2\rangle}{\partial r_i}\right]}{\partial r_i}}_{\text{Transport in scale space}}$$
$$=\underbrace{-2\langle\delta u_i\delta u_j\rangle\frac{\partial\delta U_j}{\partial r_i}-2\langle u_i^*\delta u_j\rangle\frac{\partial\delta U_j}{\partial X_i}}_{\text{Production}}\underbrace{-4\nu\left(\frac{1}{4}\left\langle\frac{\partial\delta u_j}{\partial X_i}\frac{\partial\delta u_j}{\partial X_i}\right\rangle+\left\langle\frac{\partial\delta u_j}{\partial r_i}\frac{\partial\delta u_j}{\partial r_i}\right\rangle\right)}_{\text{Dissipation}}. \tag{3.2}$$

This form is more useful because the transport terms are now written as the divergence of fluxes in the two spaces. Indeed, we can rewrite (3.2) in a compact form as

$$\frac{\partial\boldsymbol{\phi}_{\boldsymbol{s}i}}{\partial X_i}+\frac{\partial\boldsymbol{\phi}_{\boldsymbol{r}i}}{\partial r_i}=\mathcal{P}-\epsilon\equiv\mathcal{P}_{net}, \tag{3.3}$$

and define

$$\boldsymbol{\phi}_{\boldsymbol{s}i}=\underbrace{\langle U_i^*\delta q^2\rangle}_{=\phi_{s_i}^M}+\underbrace{\langle u_i^*\delta q^2\rangle}_{=\phi_{s_i}^F}+\underbrace{\langle 2\delta u_i\delta p\rangle}_{=\phi_{s_i}^P}\underbrace{-\frac{1}{2}\nu\frac{\partial\langle\delta q^2\rangle}{\partial X_i}}_{=\phi_{s_i}^V} \tag{3.4}$$

as the flux vector in physical space and

$$\boldsymbol{\phi}_{\boldsymbol{r}i}=\underbrace{\langle\delta u_i\delta q^2\rangle}_{=\phi_{r_i}^F}+\underbrace{\langle\delta U_i\delta q^2\rangle}_{=\phi_{r_i}^M}\underbrace{-2\nu\frac{\partial\langle\delta q^2\rangle}{\partial r_i}}_{=\phi_{r_i}^V} \tag{3.5}$$

as the flux vector in scale space. As before,

$$\mathcal{P}=-2\langle\delta u_i\delta u_j\rangle\frac{\partial\delta U_j}{\partial r_i}-2\langle u_i^*\delta u_j\rangle\frac{\partial\delta U_j}{\partial X_i} \tag{3.6}$$

is the production term and

$$\epsilon=4\nu\left(\frac{1}{4}\left\langle\frac{\partial\delta u_j}{\partial X_i}\frac{\partial\delta u_j}{\partial X_i}\right\rangle+\left\langle\frac{\partial\delta u_j}{\partial r_i}\frac{\partial\delta u_j}{\partial r_i}\right\rangle\right)=2\left(\epsilon^+{+}\epsilon^-\right)=4\epsilon^* \tag{3.7}$$

is the dissipation term. In the above equation, $\epsilon^+=\nu\langle(\partial u_j^+/\partial x_i^+)(\partial u_j^+/\partial x_i^+)\rangle$ and $\epsilon^-=\nu\langle(\partial u_j^-/\partial x_i^-)(\partial u_j^-/\partial x_i^-)\rangle$ are the local dissipations at points x_i^+ and x_i^-, respectively, while $\epsilon^*=(\epsilon^++\epsilon^-)/2$ is the midpoint value. Note that in (3.3) we have also defined the net production as $\mathcal{P}_{net}=\mathcal{P}-\epsilon=\mathcal{P}-4\epsilon^*$.

In (3.4) and (3.5) we have decomposed the flux vectors into constituent components due to mean flow, turbulent fluctuations, pressure and viscous diffusion; these are denoted with superscripts $\boldsymbol{M}$, $\boldsymbol{F}$, $\boldsymbol{P}$ and $\boldsymbol{V}$, respectively, i.e. $\boldsymbol{\phi_s}=\boldsymbol{\phi_s^M}+\boldsymbol{\phi_s^F}+\boldsymbol{\phi_s^V}+\boldsymbol{\phi_s^P}$ and $\boldsymbol{\phi_r}=\boldsymbol{\phi_r^M}+\boldsymbol{\phi_r^F}+\boldsymbol{\phi_r^V}$. In summary, we have four flux vector pairs arising from different mechanisms: $(\boldsymbol{\phi_s^M},\boldsymbol{\phi_r^M})$, $(\boldsymbol{\phi_s^F},\boldsymbol{\phi_r^F})$, $(\boldsymbol{\phi_s^V},\boldsymbol{\phi_r^V})$, $(\boldsymbol{\phi_s^P},0)$. Note that if we define $p^*=(p^++p^-)/2$ as the midpoint value of the fluctuating pressure, it is easy to prove that $2(\partial\langle\delta u_i\delta p\rangle/\partial X_i)=8(\partial\langle\delta u_i p^*\rangle/\partial r_i)$, so the pressure–velocity correlation term can be

https://doi.org/10.1017/jfm.2022.285 Published online by Cambridge University Press

written in flux divergence form in either physical or scale space (here we write this term in physical space).

It is possible to write (3.3) in an even more compact form as

$$\frac{\partial \boldsymbol{\phi}_{\boldsymbol{\xi}\, i}}{\partial \xi_i} = \mathcal{P} - 4\epsilon^*, \tag{3.8}$$

where $\xi = (x_1, x_2, x_3, r_1, r_2, r_3)$ is the composite position vector and $\boldsymbol{\phi}_{\boldsymbol{\xi}}(\xi) = (\phi_{s1}, \phi_{s2}, \phi_{s3}, \phi_{r1}, \phi_{r2}, \phi_{r3})$ is a six-dimensional flux vector, with each component depending on ξ.

In the flow considered in this paper, only the spanwise direction x_3 is homogeneous, so averaging is performed in time and along x_3. The composite position vector ξ and the flux vector $\boldsymbol{\phi}_{\boldsymbol{\xi}}(\xi)$ thus become five-dimensional, i.e.

$$\xi = (x_1, x_2, r_1, r_2, r_3) \quad \text{and} \quad \boldsymbol{\phi}_{\boldsymbol{\xi}}(\xi) = (\phi_{s1}, \phi_{s2}, \phi_{r1}, \phi_{r2}, \phi_{r3}). \tag{3.9a,b}$$

Due to this high dimensionality judicious choices must be made in the selection of the projection hyper-planes that will allow the extraction of the maximum amount of information. In the present paper, we project the flux vector to the two-dimensional planes $(r_3, x_2 = Y)$, $(r_1, x_2 = Y)$ and the three-dimensional hyper-plane $(r_1, r_3, x_2 = Y)$, i.e. we plot (ϕ_{r3}, ϕ_{s2}), (ϕ_{r1}, ϕ_{s2}) and $(\phi_{r1}, \phi_{r3}, \phi_{s2})$ at several streamwise locations x_1. For all cases, we have assumed that the separation in the wall-normal direction is $r_2 = 0$.

In the Appendix we provide evidence that the computed fields balance the KHMH equation. In figures 18 and 19 we plot the variation of the budget terms in the wall-normal direction for two streamwise locations, *TR*2 and *TU*, and two pairs of separations. As can be seen, the equation is balanced very well; the residual is at most a few percentage points of maximum production. Similar results were found for other locations and streamwise/spanwise separations.

We close this section by mentioning that as the separation increases, i.e. $|r_i| \to \infty$, the velocity correlation $\langle u_i^+ u_i^- \rangle \to 0$ and therefore $\langle \delta q^2 \rangle \to 2(k^+ + k^-)$, where $k^+ = \frac{1}{2}\langle u_i^+ u_i^+ \rangle$ and $k^- = \frac{1}{2}\langle u_i^- u_i^- \rangle$ are the TKEs at points x_i^+ and x_i^-, respectively. Thus for large separations, the asymptotic form of (3.2) is twice the sum of the TKE transport equations (2.1) applied at each point. Both the nonlinear interscale transfer $\partial \langle \delta u_i \delta q^2 \rangle / \partial r_i$ and the turbulent advection $\partial \langle ((u_i^+ + u_i^-)/2) \delta q^2 \rangle / \partial X_i$ tend to

$$\frac{1}{2}\left(\frac{\partial}{\partial x_i^+} \langle u_i^+ u_j^+ u_j^+ \rangle + \frac{\partial}{\partial x_i^-} \langle u_i^- u_j^- u_j^- \rangle \right) \tag{3.10}$$

as $|r_i| \to \infty$, thus both contribute equally to the turbulent diffusion term of the TKE equation.

4. Energy fluxes on the (r_3, Y) plane

4.1. *General characteristics*

Figure 5 shows the evolution of the flux vector components $(\boldsymbol{\phi}_{r3}, \boldsymbol{\phi}_{s2})$ in the (r_3, Y) plane (with $r_1 = 0$) from the laminar to turbulent region. Wall-normal distances and separations are normalised by the local wall variables (left and bottom axes) and global variables (top and right axes). The pink dashed line indicates the local boundary layer thickness. In order to facilitate the interpretation of these plots, we also superimpose coloured contours of the net production, $\mathcal{P}_{net} = \mathcal{P} - \epsilon$.

https://doi.org/10.1017/jfm.2022.285 Published online by Cambridge University Press

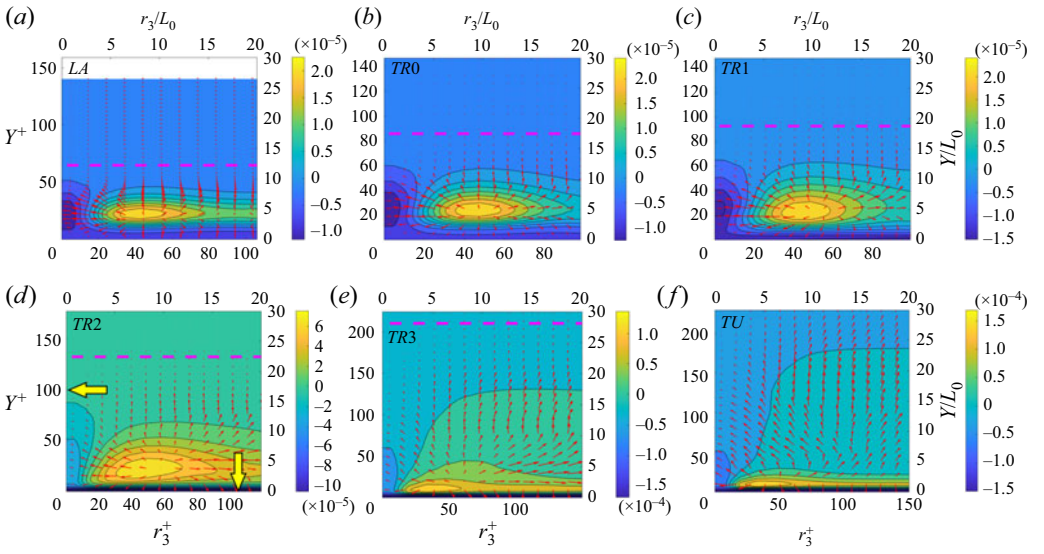


Figure 5. (*a–f*) Evolution of energy flux vector ($\boldsymbol{\phi}_{r3}, \boldsymbol{\phi}_{s2}$) on ($r_3, Y$) plane (red arrows) from laminar to turbulent region. The coloured contour is the net production (normalised with global variables) and the pink dashed lines indicate the local boundary layer thickness. The yellow arrows in (*d*) point to the two sink regions, $r_3 = 0$ and $Y = 0$. The maximum vector magnitude (corresponding to the longest arrow on each plot) is 5×10^{-5}, 7.6×10^{-5}, 9.1×10^{-5}, 1.7×10^{-4}, 2.4×10^{-4}, 2.2×10^{-4} from *LA* to *TU*, respectively.

At all spatial locations $\mathcal{P}_{net}$ peaks at particular r_3 separations and wall-normal distances Y (the peaks appear as concentrated yellow regions). The production $\mathcal{P}$ arises from the inhomogeneity of the time-average flow in the physical and scale spaces, as evidenced by the two terms in (3.6). We analysed the contribution of each term and found that the large production arises due to the inhomogeneity in scale space, and in particular from the component $-2\langle\delta u_2 \delta u_1\rangle \partial \delta U_1/\partial r_2|_{r_2=0}$. The contribution of the second term is exactly 0 (due to the spanwise homogeneity of the time-average flow). It is easier to understand the physical mechanism that leads to high production if we focus on the laminar region (figure 5*a*). In this region Klebanoff modes (laminar streaks) are present that result in positive and negative streamwise velocity fluctuations; therefore δu_1 is maximised when r_3 is equal to the distance between two streaks. The wall-normal fluctuation differences δu_2 are also maximised at the same distance (refer to figure 24 in Xiao & Papadakis (2019)) resulting in large time and spanwise averages $\langle\delta u_2 \delta u_1\rangle$. The shear rate in scale space can be written as

$$\frac{\partial \delta U_1}{\partial r_2} = \frac{1}{2}\left(\frac{\partial \delta U_1}{\partial x_2^+} - \frac{\partial \delta U_1}{\partial x_2^-}\right) = \frac{1}{2}\left(\frac{\partial U_1^+}{\partial x_2^+} + \frac{\partial U_1^-}{\partial x_2^-}\right) \tag{4.1}$$

and due to spanwise homogeneity of U_1 and the fact that $r_2 = 0$ (meaning that $x_2^+ = x_2^- = x_2 = Y$, thus $U_1^+ = U_1^- = U_1$) this can be simplified to $\partial \delta U_1/\partial r_2|_{r_2=0} = \partial U_1/\partial x_2$. The production term can therefore be written as $\mathcal{P} = -2\langle\delta u_2 \delta u_1\rangle \partial U_1/\partial x_2$. The corresponding term for the TKE equation is $\mathcal{P}_k \approx -\langle u_2 u_1\rangle \partial U_1/\partial x_2$, which is of course uniform in the spanwise direction (see figure 3*b*). The peak production location of the KHMH equation in the (r_3, Y) plane is therefore determined by the spanwise distance between the Klebanoff modes and the wall-normal distance at which the product of the second-order structure function $\langle\delta u_2 \delta u_1\rangle$ and the shear $\partial U_1/\partial x_2$ is maximum. The mean flow therefore

https://doi.org/10.1017/jfm.2022.285 Published online by Cambridge University Press

injects energy at a specific r_3 separation, which is determined by the receptivity process arising from the interaction between free-stream turbulence forcing and shear during the early development of the boundary layer. This process controls the spacing between the Klebanoff modes, which is of the order of the boundary layer thickness close to the inlet.

As the flow evolves, the location of peak net production changes smoothly and approaches the wall. The largest energy production appears at the *TU* location, inside the buffer layer, at $Y^+ \approx 12$ and $r_3^+ \approx 40$, consistent with the results of Cimarelli *et al.* (2015) for channel flow. The large production at specific regions in the (r_3, Y) plane strongly affects the energy transfer in the physical and scale spaces, to which we now turn.

For all streamwise locations the energy fluxes originate from the $\mathcal{P}_{net}$ peak location and radiate outwards. In the laminar region (*LA*), most of the energy produced flows to smaller r_3 scales and is dissipated (forward cascade). There is weak inverse cascade to larger r_3 scales, while the energy flux in the wall-normal direction is negligible. At the turbulent region (*TU*) the fluxes show a different behaviour. The energy injected from the time-average flow radiates in all directions. There are two sinks indicated by yellow arrows in the *TR*2 plot of figure 5; one towards the wall (where it is dissipated) and the other towards small r_3 scales (indicating a forward cascade). An inverse energy cascade also appears, i.e. energy flows to larger r_3 scales to the right of the $\mathcal{P}_{net}$ before most of the flux vectors then change direction and bend towards the Y axis ($r_3 = 0$). This map is very similar to that of turbulent channel flow (Cimarelli *et al.* 2013, 2015, 2016).

In the transition region, the scale energy transfer pattern morphs progressively from laminar to turbulent shape. Downstream of *TR*0, the energy flux in the wall-normal direction (i.e. towards the bulk of the flow) energises the region above the Klebanoff modes, increasing the thickness of the boundary layer. This indicates that the equilibrium boundary layer at *TU* is forming gradually during the transition process. Significant inverse cascade appears towards larger r_3 scales, but it is noteworthy that the bending of the energy flux vectors towards small scales does not appear in the transition region, but only at the *TU* region. It seems that strong inverse cascade is a central characteristic of transition; we will elaborate more on this important feature again later.

In order to shed more light onto the patterns shown in figure 5, we turn our attention to the decompositions (3.4) and (3.5) and investigate the contributions of fluxes due to mean flow, nonlinear interactions, viscosity and pressure.

4.2. *Analysis of decomposed energy fluxes*

We focus in particular on the *TR*2 location, in the middle of the transition region. In figure 6 we plot the four pairs of fluxes $(\boldsymbol{\phi}^F_{r_3}, \boldsymbol{\phi}^F_{s_2})$, $(\boldsymbol{\phi}^V_{r_3}, \boldsymbol{\phi}^V_{s_2})$, $(\boldsymbol{\phi}^M_{r_3}, \boldsymbol{\phi}^M_{s_2})$ and $(\boldsymbol{0}, \boldsymbol{\phi}^P_{s_2})$ in the (r_3, Y) plane; these are denoted with $\boldsymbol{F}$, $\boldsymbol{V}$, $\boldsymbol{M}$ and $\boldsymbol{P}$, respectively. We also plot the sum $(\boldsymbol{\phi}^F_{r_3} + \boldsymbol{\phi}^V_{r_3}, \boldsymbol{\phi}^F_{s_2} + \boldsymbol{\phi}^V_{s_2})$, denoted as $\boldsymbol{F} + \boldsymbol{V}$, and the total flux $(\boldsymbol{\phi}_{r3}, \boldsymbol{\phi}_{s2})$, which is of course identical to that shown in figure 5(*d*). In all plots, the flux vectors are plotted as arrows to show the direction, but we also superimpose the flux magnitude as contours.

We first note that the fluxes due to mean flow and pressure have components only in physical space, i.e. the wall-normal direction; this is because $\boldsymbol{\phi}^P_{r_3} = 0$ and $\boldsymbol{\phi}^M_{r_3} = \langle \delta U_i \delta q^2 \rangle = 0$ due to homogeneity in the spanwise direction. Therefore in the r_3 direction the fluxes are due to the nonlinear and viscous terms only, $\boldsymbol{\phi}^F_{r_3}$ and $\boldsymbol{\phi}^V_{r_3}$. The latter term results in forward cascade, while the former transfers energy to larger scales (inverse cascade) and to the bulk of the flow. The superposition of these two terms results in the $\boldsymbol{F} + \boldsymbol{V}$ pattern, which is almost identical to the total in the r_3 direction. Adding the contribution of pressure and mean flow terms, which both transfer energy towards the

https://doi.org/10.1017/jfm.2022.285 Published online by Cambridge University Press

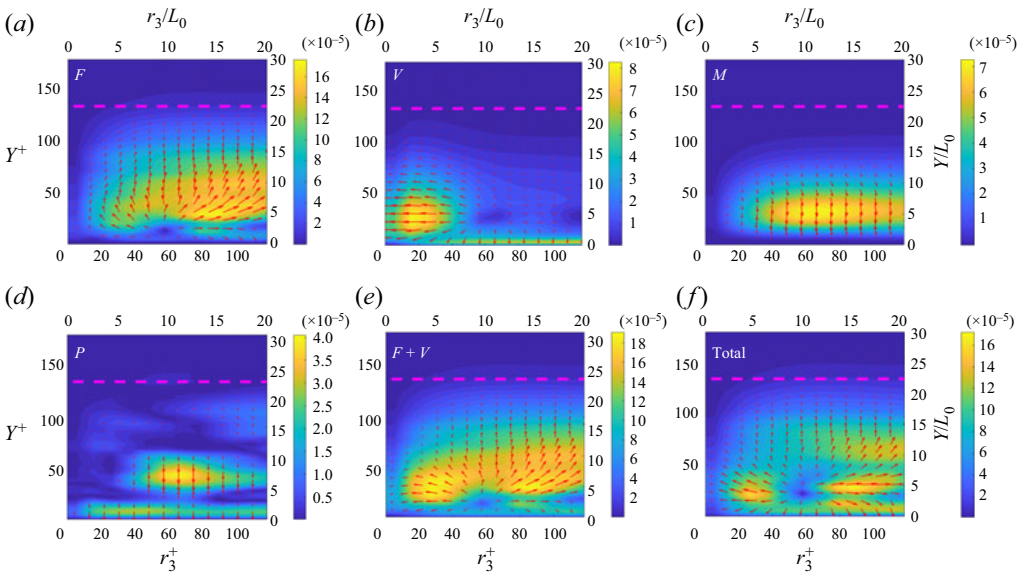


Figure 6. Maps of flux vectors due to nonlinear interaction between (*a*) velocity fluctuations (F), (*b*) viscosity (V), (*c*) mean velocity (M), (*d*) pressure (P), (*e*) combination ($F + V$) and (*f*) total on (r_3, Y) plane at *TR*2 location. Contours represent the magnitude of the corresponding flux vectors.

wall, readjusts the direction of the arrows, and completes the picture. The readjustment is especially evident at $Y \approx 5L_0$, and results in almost horizontal total inverse fluxes.

In figure 7 we plot the evolution of the two most important terms (viscous and nonlinear) at all streamwise locations. For comparison purposes, we also include the total flux in the same plot (right-hand column). We first notice that the viscous flux (middle column) results mainly in forward cascade (but there are some regions of very weak inverse cascade) and energy towards the wall. As transition progresses, the forward cascade acts at progressively smaller scales, while the energy transfer towards the wall becomes stronger. The latter is firmly established over a wide range of scales in the viscous sublayer when the turbulent region is reached. The viscous effect can be clearly seen also on the total energy flux plots, especially in the *TR*3 and *TU* locations. The energy transfer due to the nonlinear interaction term is more involved. This term mainly acts to transfer energy to larger scales (inverse cascade) and this is evident at all streamwise locations, even in the laminar (*LA*) region (but it is quite weak there). Starting from the *TR*0 location, it also acts to transfer energy to the bulk of the flow. The radial flux pattern that appears in the total flux plots (right-hand column) is thus due to the superposition of the effects of the nonlinear interaction and viscous terms.

We now turn our attention to energy transfer in the (r_1, Y) plane.

5. Energy fluxes on the (r_1, Y) plane

For each streamwise location, we select the r_3 value that corresponds to the peak net production shown in figure 5; the resulting separations are $r_3/L_0 = 8, 8, 8, 8, 5, 5$ at positions *LA*, *TR*0, *TR*1, *TR*2, *TR*3, *TU*, respectively. This allows us to investigate the behaviour of the energy fluxes at the particular r_3 separation at which the energy due the mean shear is injected.

https://doi.org/10.1017/jfm.2022.285 Published online by Cambridge University Press

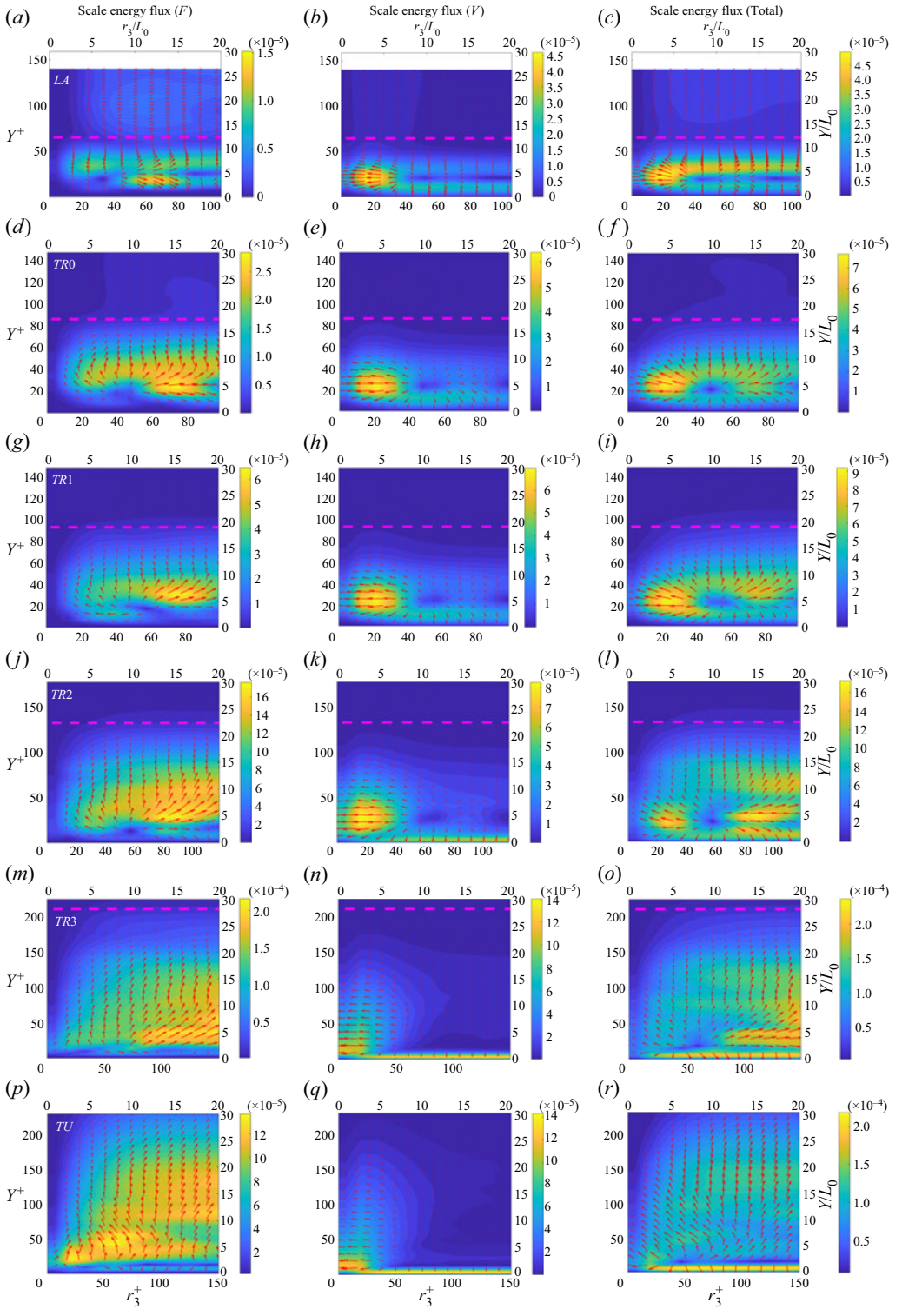


Figure 7. Evolution of energy fluxes due to the nonlinear interaction term (*a*,*d*,*g*,*j*,*m*,*p*) and the viscous term (*b*,*e*,*h*,*k*,*n*,*q*) in the (r_3, Y) plane. (*c*,*f*,*i*,*l*,*o*,*r*) The total flux. Contours represent the magnitude of the corresponding flux vectors. The pink dashed line is the local boundary layer thickness.

https://doi.org/10.1017/jfm.2022.285 Published online by Cambridge University Press

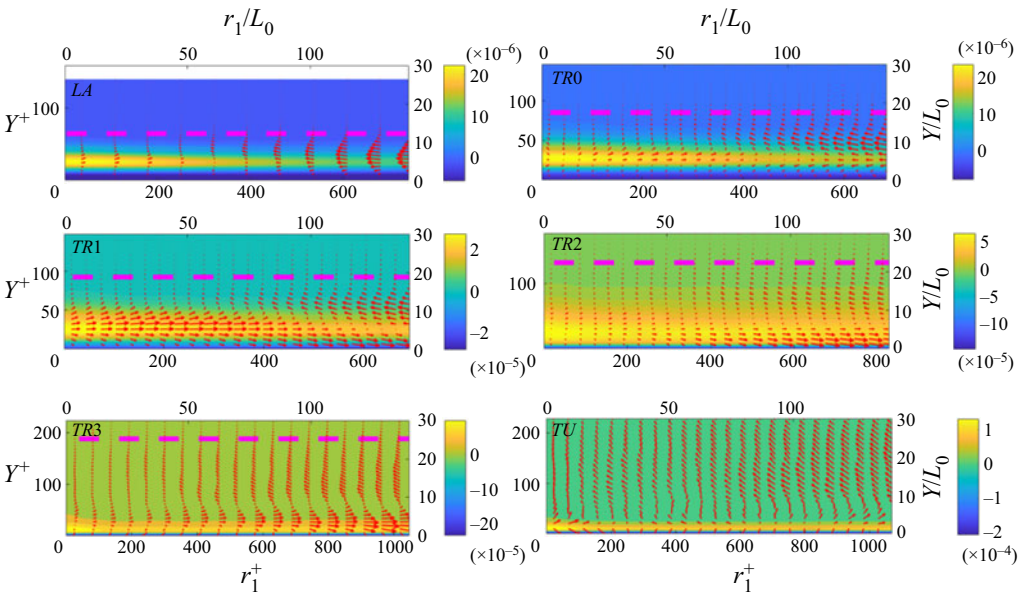


Figure 8. Evolution of the energy flux vector $(\boldsymbol{\phi}_{\boldsymbol{r}1}, \boldsymbol{\phi}_{\boldsymbol{s}2})$ on (r_1, Y) plane from laminar to turbulent region (red vectors). The contour values correspond to net production, and the pink dashed lines indicate the local boundary layer thickness. For $LA, TR0, TR1, TR2, TR3, TU$ locations, the separations are $r_3/L_0 = 8, 8, 8, 8, 5, 5$, respectively; these correspond to the peak net production shown in figure 5. The maximum vector magnitude (corresponding to the longest arrow in each plot) is 5×10^{-4}, 2.5×10^{-4}, 6×10^{-4}, 1×10^{-3}, 8×10^{-4}, 3.5×10^{-4} from LA to TU, respectively.

5.1. *General characteristics*

Figure 8 shows the evolution of the energy flux vector $(\boldsymbol{\phi}_{\boldsymbol{r}1}, \boldsymbol{\phi}_{\boldsymbol{s}2})$ on this plane. A core region of strong net production, indicated by yellow colour, can be clearly seen; this region persists throughout transition. At the LA location, this region is concentrated at small r_1 values, $0 < r_1/L_0 < 75$, but as transition progresses, it moves closer to the wall and it is elongated. Gradually, it occupies the whole range of r_1 separations considered, $0 < r_1/L_0 < 150$. Note also that apart from the first two locations LA and $TR0$, net production can take negative values very close to the wall (because of strong dissipation).

From the high production region, energy flux vectors emanate with $\boldsymbol{\phi}_{\boldsymbol{r}3} > 0$, indicating inverse cascade. At LA and $TR0$ locations this is barely noticeable, but at $TR1$ it is very strong in the region $0 < r_1/L_0 < 100$. It is also present at the downstream locations $TR2$ and $TR3$ but at larger separations, $75 < r_1/L_0 < 150$, and closer to the wall. It is very interesting to notice that once transition is complete, the inverse cascade is significantly subdued. Indeed, we can barely see it in the TU region (although the strong net production region can still be seen very clearly). In the next section we probe in more depth the origin of this inverse cascade, by examining the evolution of the different components of the energy flux.

5.2. *Decomposition of the energy fluxes*

In the (r_3, Y) plane it was found that the nonlinear interaction and viscous components of the energy flux were the most dominant. In the (r_1, Y) plane, however, the viscous component is much less important, while energy flux due to mean flow, $\phi_{r_1}^M = \langle \delta U_1 \delta q^2 \rangle$,

https://doi.org/10.1017/jfm.2022.285 Published online by Cambridge University Press

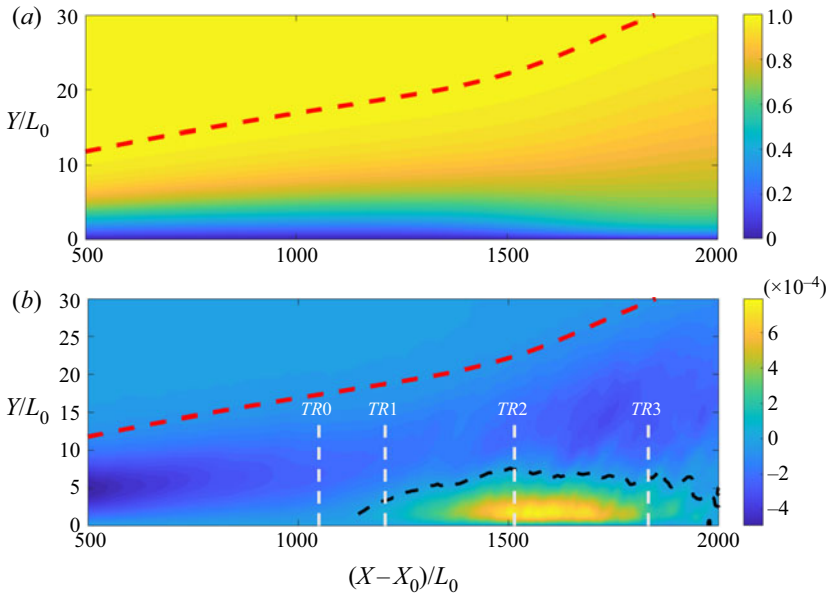


Figure 9. Contour plots of the mean streamwise velocity U_1 (a) and the normal strain rate $\mathrm{d}U_1/\mathrm{d}X_1$ (b). The black dashed curve denotes the $\mathrm{d}U_1/\mathrm{d}X_1 = 0$ isoline. The red dashed line indicates the boundary layer thickness.

assumes a more significant role. This is expected due to the strong streamwise inhomogeneity of the flow in the transition region. The sign of $\phi^M_{r_1}$ is determined by δU_1. In order to facilitate the interpretation of the results, contours of U_1 are shown in figure 9(a). For small r_1, δU_1 has the same sign as the normal strain rate $\partial U_1/\partial x_1$, thus contours of the latter are also shown in figure 9(b). In the transition region between $TR1$ and $TR3$, a zone of accelerating flow appears close to the wall, in agreement with the rise of C_f shown in figure 1. In the laminar region the flow decelerates, with the strongest negative strain around the centre of the boundary layer.

The evolution of the mean (M) and nonlinear interaction (F) components of the energy flux are shown in figure 10. Note the competition between the two components, which is quite subtle. In the laminar region LA, $\delta U_1 < 0$ and the energy flux due to the mean flow leads to forward cascade; however, the nonlinear interaction leads to inverse cascade. The two contributions cancel each other out, and this explains why the total flux shown in the top left-hand panel of figure 8 is very weak for $0 < r_1/L_0 < 75$. At $TR0$, C_f has a minimum and $\delta U_1 \approx 0$ for small r_1, but for larger separations $\delta U_1 > 0$, consistent with the steeper rise of C_f at the start of transition. Again at this location the two components compete, with $\phi^M_{r_1} < 0$ (forward cascade) and $\phi^F_{r_1} > 0$ (inverse cascade). At $TR1$, δU_1 changes sign across the boundary layer ($\delta U_1 < 0$ away from the wall and $\delta U_1 \geq 0$ close to it; refer to figure 9), but $\phi^F_{r_1} > 0$ always, leading to overall strong inverse cascade. At $TR2$ and $TR3$, $\delta U_1 > 0$ close to the wall and very weak further away, while $\phi^F_{r_1}$ exhibits a mixture of forward and inverse cascade. Finally at TU, $\delta U_1 < 0$ away from the wall for large separations (due to the growth of the boundary layer thickness), while again $\phi^F_{r_1}$ does not exhibit a clear behaviour. It is evident therefore, that at least in the earlier stages of transition, a strong inverse cascade process exists, which is predominately due to the nonlinear interaction term.

https://doi.org/10.1017/jfm.2022.285 Published online by Cambridge University Press

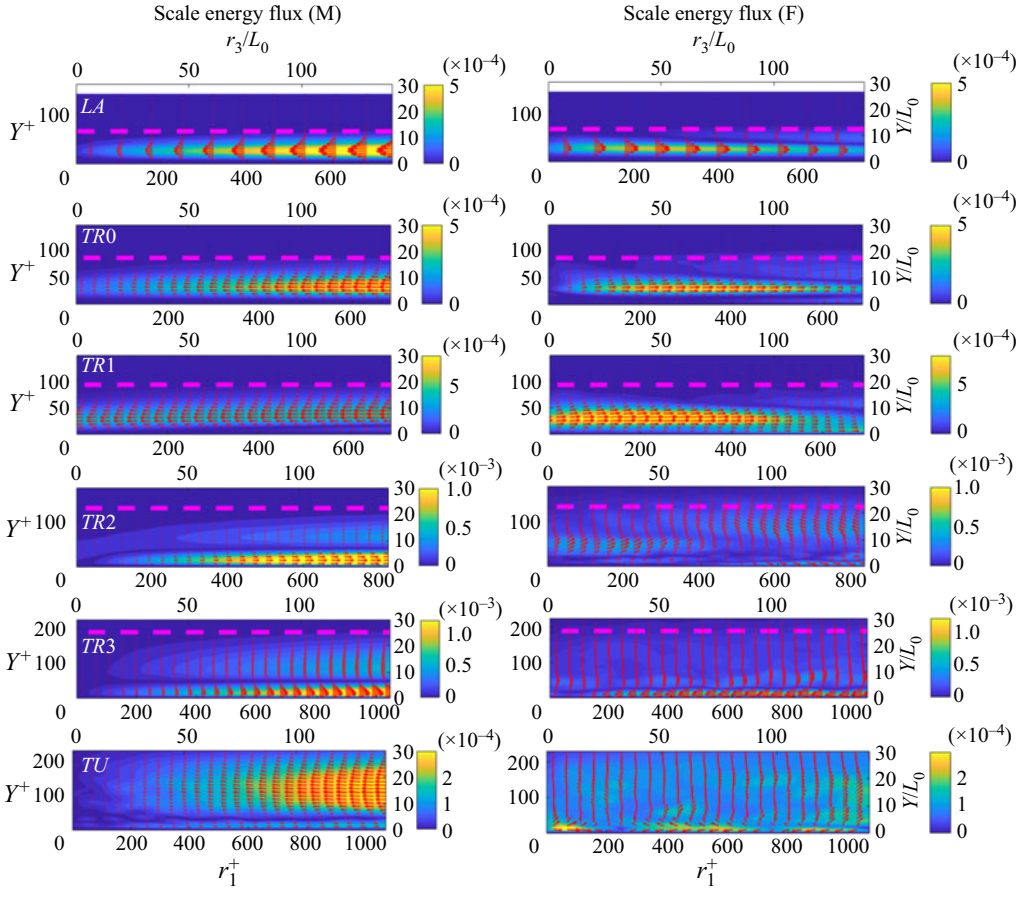


Figure 10. Evolution of the mean (M) and nonlinear interaction (F) components of the energy flux (red vectors) on the (r_1, Y) plane. The contours are the magnitude of the corresponding flux vector. The spanwise separations are $r_3/L_0 = 8, 8, 8, 8, 5, 5$ from *LA* to *TU*, respectively.

6. Energy fluxes in the (r_1, r_3) plane

In figure 11 maps of the scale energy flux vectors $(\boldsymbol{\phi}_{r1}, \boldsymbol{\phi}_{r3})$ in the (r_1, r_3) plane at four streamwise locations are shown; the wall-normal distances correspond to the peak $\mathcal{P}_{net}$ of figure 5. Contours of the net energy production are also superimposed. Figure 11(*a*) confirms the strong inverse cascade at regions of high $\mathcal{P}_{net}$, namely $5 < r_3/L_0 < 15$. It is clear that the inverse cascade is mainly directed towards the r_1 direction; in the r_3 direction it appears only for $r_3/L_0 > 10$, in agreement with figure 5, but it is much weaker. A recirculation pattern in the flow of energy is also evident, i.e. energy emanating from the large net production region flows to large r_1 and then recirculates back to small r_1 and r_3 scales. This recirculation look is much more clear in locations *TR*2 and *TU*. In *TR*3 it is not so evident, possibly because of the narrow range of the r_1 and r_3 separations considered.

7. Maps of energy flux in the three-dimensional (r_1, r_3, Y) hyper-plane

In the previous sections we examined the evolution of the energy fluxes on the two-dimensional planes (r_3, Y), (r_1, Y) and (r_1, r_3). The most significant finding is that during the transition, a strong inverse cascade of energy exists that originates from the net

https://doi.org/10.1017/jfm.2022.285 Published online by Cambridge University Press

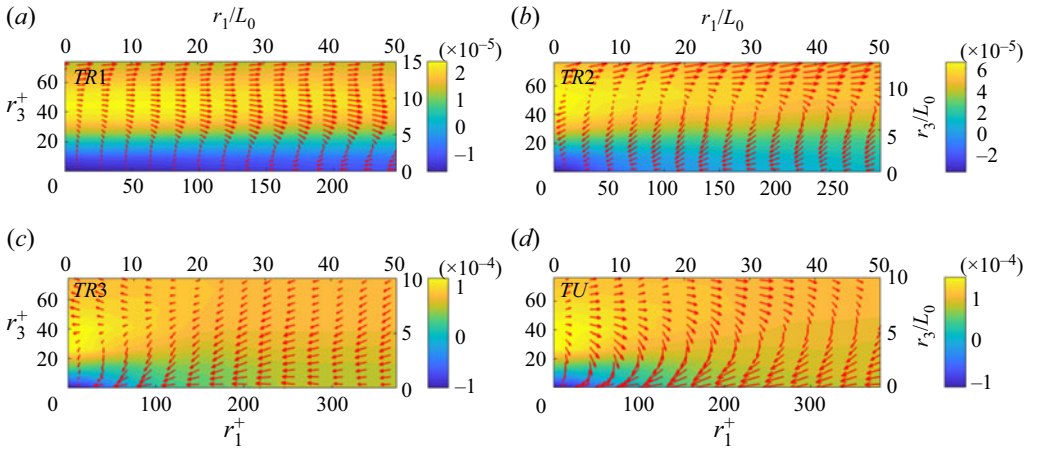


Figure 11. Scale energy flux vectors $(\boldsymbol{\phi}_{\boldsymbol{r}1}, \boldsymbol{\phi}_{\boldsymbol{r}3})$ on (r_1, r_3) plane at $Y/L_0 = 5$ for (*a*) *TR*1 and (*b*) *TR*2; $Y/L_0 = 1.3$ for (*c*) *TR*3 and (*d*) *TU* (red arrows). Contour plots of net production are superimposed. The maximum vector magnitude (corresponding to the longest arrow on each plot) is 4.5×10^{-4}, 1×10^{-3}, 6×10^{-4}, 7×10^{-4} from *TR*1 to *TU*, respectively.

production peak region and is mainly directed along the r_1 direction. However, previous results provide only limited understanding because they are visualised on two-dimensional planes, so in this section, we map the energy paths on the three-dimensional hyper-plane (r_1, r_3, Y). These maps are shown in figure 12 for three streamwise locations *LA*, *TR*2 and *TU*, and are visualised from two different viewing angles. To aid understanding, we also superimpose the isosurface $0.7 \max(\mathcal{P}_{net})$ in yellow colour. For *TR*2 and *TU* we focus on different areas of the map; we do this by plotting the stream-tubes crossing small spheres placed at different r_1 separations (refer to the figure legend for more details).

In the laminar (*LA*) and transition (*TR*2) regions, the net production region (in yellow colour) is centred at $r_3 = 10L_0$, $Y = 5L_0$ and is elongated in the r_1 direction. At *TU*, this region moves closer to the wall ($r_3 = 5L_0$, $Y = 1.3L_0$) and significantly shrinks in the streamwise direction (r_1). In all three locations, energy stream-tubes emanate from the production region but their behaviour is different. In the laminar (*LA*) region, a weak inverse cascade along the r_1 direction is observed and then the flow energy pathlines bend upwards to the bulk of the flow and downwards to the wall region. At *TR*2, the energy flux is an order of magnitude larger compared with that at *LA*. Very strong inverse cascade is present in the r_1 direction, consistent with figures 8 and 11, but the energy paths then bend back to small r_1 and r_3 and towards the bulk of the flow; this explains the recirculating pattern noticed in figure 11. In the turbulent *TU* region, there is still inverse cascade in the r_1 direction, but it is weaker and confined to a smaller r_1 domain. Again, once energy has travelled for a sufficient distance in the r_1 direction, the stream-tubes bend to smaller r_1 and r_3 scales and to the bulk of the flow. The flux map at this location is very similar to that of channel flow (Cimarelli *et al.* 2013).

8. Analysis of instantaneous interscale energy fluxes in physical space

The analysis presented in the previous sections identified a strong inverse cascade close to the wall, at wall-normal locations $Y < 10L_0$, which is mainly directed in the streamwise direction. In this section, we relate the energy transfer to the physical processes that take place during transition, and in particular to the growth of turbulent spots.

https://doi.org/10.1017/jfm.2022.285 Published online by Cambridge University Press

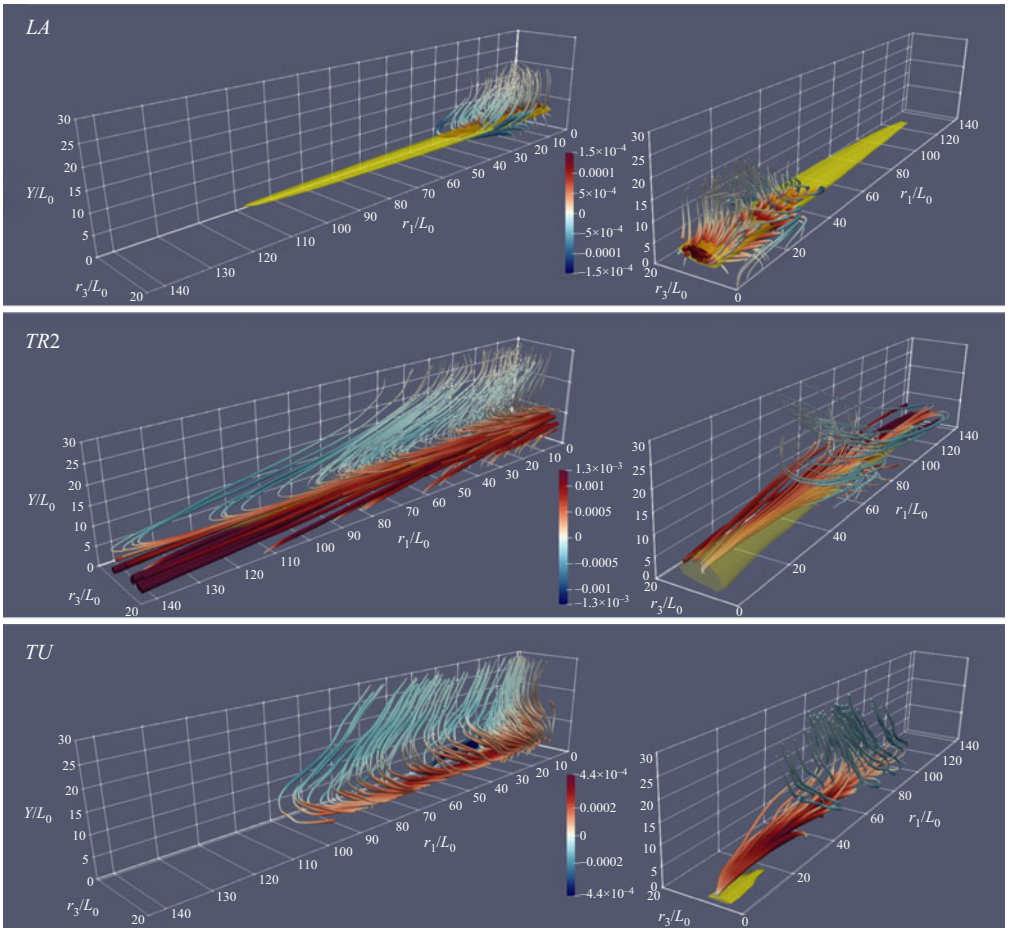


Figure 12. Maps of energy flux in the three-dimensional (r_1, r_3, Y) hyper-plane in the form of stream-tubes for three streamwise locations. The yellow isosurface denotes $0.7\max(\mathcal{P}_{net})$. The stream-tubes are coloured according to the sign of ϕ_{r_1} (red for positive, blue for negative, thus indicating inverse and forward cascade, respectively). The colour bar refers to the value of ϕ_{r_1}. The radius of the tubes grows with increasing magnitude of the flux vector. Each plot was generated by placing a sphere at a specific location and tracing the stream-tubes crossing the sphere. For *LA*, a sphere of radius $15L_0$ is placed at $(r_1 = 5L_0, r_3 = 7.5L_0, Y = 5L_0)$ (left and right columns show the same stream-tubes from different angles). For *TR*2, a sphere of radius $30L_0$ is placed at two points ($r_1 = 20L_0$ and $70L_0$, $r_3 = 7.5L_0$, $Y = 5L_0$) (left column) and at $(r_1 = 70L_0, r_3 = 7.5L_0, Y = 5L_0)$ (right column). For *TU*, a sphere of radius $30L_0$ is placed at two points ($r_1 = 10L_0$ and $60L_0$, $r_3 = 7.5L_0$, $Y = 1.3L_0$) (left column) and at $(r_1 = 60L_0, r_3 = 7.5L_0, Y = 1.3L_0)$ (right column).

Figure 13 shows four snapshots of the instantaneous wall-normal velocity fluctuation at $Y = 1.3L_0$; the time delay between two snapshots is $\Delta t = 500$ time units. In figure 13(*a*), two turbulent patches are starting to form at locations $(X - X_0)/L_0 \approx 1300$ and 1400. The two patches grow and propagate downstream as shown in figure 13(*b*), and finally merge to form a large turbulent patch, which is clearly visible in figure 13(*c*). This large patch then propagates as a single entity (figure 13*d*).

We now focus our attention to the rectangular area marked with a green dashed line in figure 13(*c*), which contains both laminar and turbulent regions. This area extends between 1002 and 1502 and between 0 and 50 in the streamwise and spanwise directions, respectively, and covers the region between locations *TR*1 and *TR*2 (see markings at the

https://doi.org/10.1017/jfm.2022.285 Published online by Cambridge University Press

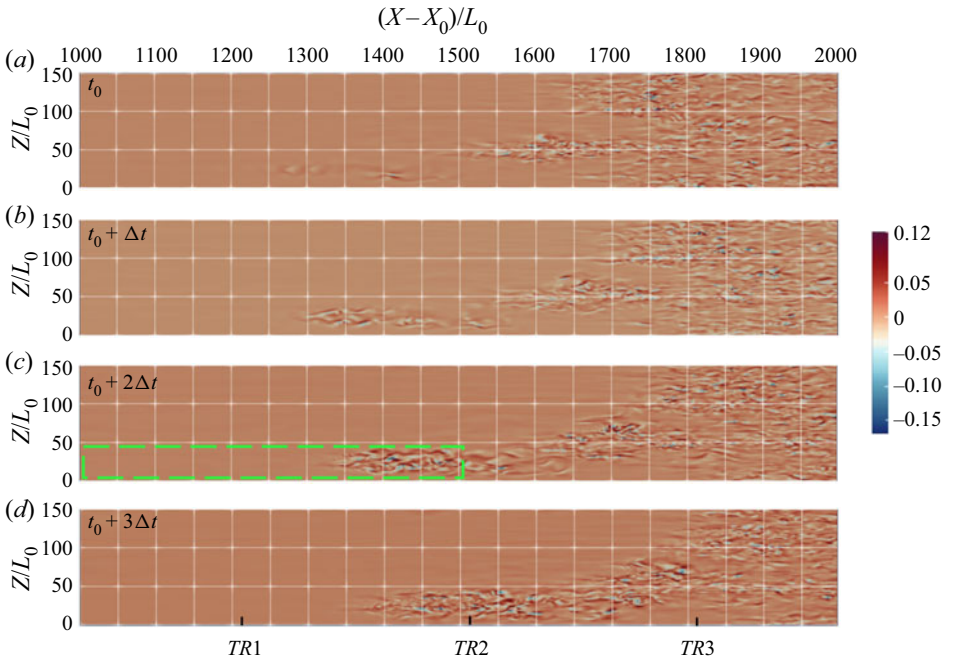


Figure 13. Contour plots of the instantaneous wall-normal velocity fluctuation at $Y = 1.3L_0$ at (a–d) four time instances. The time separation Δt between two snapshots is 500 time units.

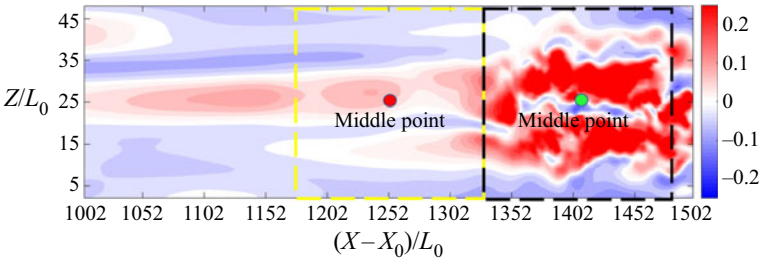


Figure 14. Contour plots of the instantaneous streamwise velocity fluctuations within the rectangular area marked with a green border in figure 13(c).

bottom of figure 13d). In figure 14 contour plots of the streamwise velocity fluctuations within the selected rectangular area are shown. We choose now two points, one red (at $(X - X_0)/L_0 = 1252$, within a laminar Klebanoff streak) and one green (at $(X - X_0)/L_0 = 1402$, within a streak that breaks down). We think of these two points as fixed middle points around which we consider separations r_1 up to $150L_0$ (consistent with figure 8) and r_3 up to $50L_0$. These separations define two regions, $[1177, 1327] \times [0, 50]$ and $[1327, 1477] \times [0, 50]$, that are marked with dashed yellow and black borders, respectively, in figure 14.

We can investigate the relation between the instantaneous flow and the scale fluxes within these two regions by plotting them in two separate figures. However the interpretation of the results is facilitated if the two figures are superimposed on a single plot. We do this in figure 15(a) for the first region $[1177, 1327] \times [0, 50]$. In this panel, we superimpose the interscale energy flux vector $(\boldsymbol{\phi}_{r1}, \boldsymbol{\phi}_{r3})$ on the (r_1, r_3) plane (top and

https://doi.org/10.1017/jfm.2022.285 Published online by Cambridge University Press

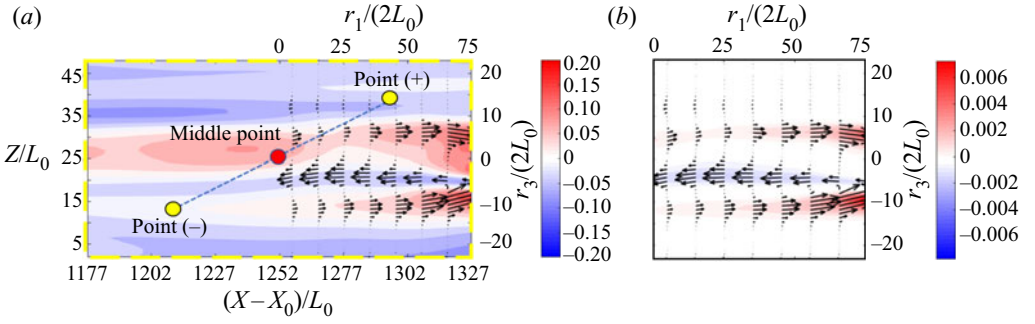


Figure 15. Contours of the streamwise velocity fluctuations (*a*) and of the energy flux component $\boldsymbol{\phi}_{\boldsymbol{r}1}$ (*b*). In both panels, the superposed black arrows indicate the direction of the energy flux vector ($\boldsymbol{\phi}_{\boldsymbol{r}1}$, $\boldsymbol{\phi}_{\boldsymbol{r}3}$). The middle point is located at $(X - X_0)/L_0 = 1252$.

right axes) together with the instantaneous streamwise fluctuations in the (X, Z) plane (left and bottom axes). The process is as follows. We select an arbitrary point $x_i^+ = X_i + r_i/2$ to the right of the middle point X_i, and find the corresponding $x_i^- = X_i - r_i/2$, as shown in the figure. We then compute the energy flux vector using the fluctuations in these two points, and place the vector at x_i^+ (and since $x_i^+ = X_i + r_i/2$, the legends of the top and right axes are $r_1/(2L_0)$ and $r_3/(2L_0)$, respectively). In this way we can relate directly the instantaneous interscale energy fluxes with the dynamics of the streak breakdown and turbulent patch formation and growth. The right-hand boundary of the area considered in figure 15 is just upstream of the streak breakdown (see also figure 14). Note the stronger streamwise velocity fluctuations when the two high-speed streaks start to break down (at $Z/L_0 \approx 10$ and ≈ 30) and the associated inverse cascade. Forward cascade is observed instantaneously around the narrow low-speed streak located in between, at $Z/L_0 \approx 20$. In figure 15(*b*), we present both the flux vectors and contours of the flux component $\boldsymbol{\phi}_{\boldsymbol{r}1}$; the contours show that the inverse cascade is relatively weak at this time instant and location.

We repeat the process for the region marked by the black border in figure 14. The middle point is now at $(X - X_0)/L_0 = 1402$ and is located firmly within the streak breakdown region. Indeed it is surrounded by two high-speed streaks that disintegrate to form a turbulent spot; the spot can be clearly seen in figure 13(*c*). The results, shown in figure 16, indicate that the large velocity fluctuations inside the streaks contribute to an inverse cascade around the middle point, and this corresponds to the growth of the high-speed streaks within the turbulent spot. Comparison of the streamwise flux components $\boldsymbol{\phi}_{\boldsymbol{r}1}$ (figures 15*b* and 16*b*) shows that the inverse cascade is much stronger when the streaks break down. This is because the interscale flux scales with the cube of velocity difference, so a small increase in δu_1 results in much larger fluxes.

In both regions considered, inverse cascade appears when the instantaneous flow accelerates between x_i^- and x_i^+. This can also seen in the average picture in figure 8. Note that the interpretation of inverse cascade for fixed values of r_3 (for example for those values where $\mathcal{P}_{net}$ is maximised, as in figure 10) refers to the growth of streaks within spots. This is of course related to the growth of spots themselves, as the latter consist of high-speed streaks that grow individually.

The analysis of the growth of spots as single entities in the spanwise direction using the KHMH formulation is possible, but it is more involved. It would require the identification of a spot using an indicator function as in Marxen & Zaki (2019) and Yao *et al.* (2020), positioning of the midpoint X_i at the centroid of the spot and integration of the KHMH

https://doi.org/10.1017/jfm.2022.285 Published online by Cambridge University Press

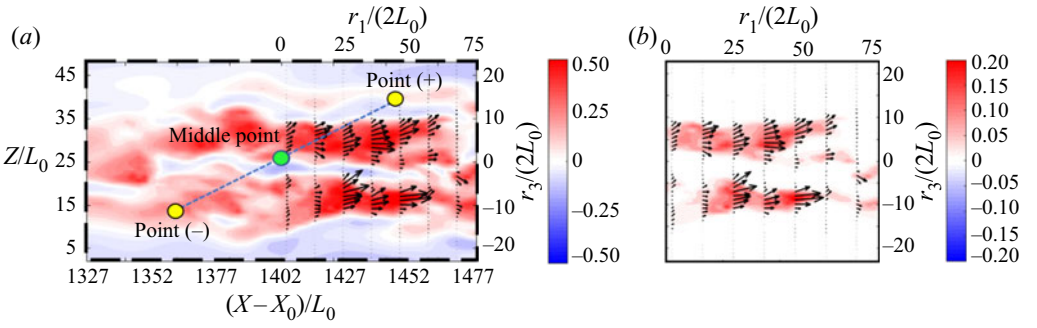


Figure 16. Contours of the streamwise velocity fluctuations (*a*) and of the energy flux component $\boldsymbol{\phi}_{\boldsymbol{r}1}$ (*b*). In both panels, the superposed black arrows indicate the direction of the energy flux vector $(\boldsymbol{\phi}_{\boldsymbol{r}1}, \boldsymbol{\phi}_{\boldsymbol{r}3})$. The middle point is located at $(X - X_0)/L_0 = 1402$.

equation in the scale space around the spot bounding surface. This is a generalisation of the integration over a sphere performed by Hill (2002) and can elucidate very clearly the mechanisms for interscale energy transfer to the spot as a single entity. This is, however, beyond the scope of the present paper.

The previous analysis demonstrated that the scale fluxes depend strongly on the distance from the wall and are highly intermittent. This motivates the investigation of their PDF. Figure 17(*a*) shows the PDFs of $\boldsymbol{\phi}_{\boldsymbol{r}_1}$ at the streamwise location *TR*1 for fixed separation $(r_1, r_3) = (50L_0, 8L_0)$ and three different wall-normal distances. We also plot the PDFs of the components $\phi^M_{r_1} = \delta U_1 \delta q^2$ (figure 17*b*) and $\phi^F_{r_1} = \delta u_1 \delta q^2$ (figure 17*c*). In total 55 000 time and spanwise samples were used to construct these PDFs. Although this is not ideal, because spanwise samples smooth out the fluxes around localised spots shown in figure 13, the PDFs still provide a more complete picture compared with time averages.

At the separations considered there is strong inverse cascade, as shown in figure 8. At $Y = 7L_0$, where the inverse cascade is maximised, the shape of the PDF of $\boldsymbol{\phi}_{\boldsymbol{r}_1}$ is slightly asymmetric and skewed towards positive values. At the other two locations, the PDF is nearly symmetric resulting in very low time averages. The PDFs of $\phi^M_{r_1}$ are one-sided; the sign depends on δU_1 and varies with wall-normal distance. This results in a competition between $\phi^F_{r_1}$ and $\phi^M_{r_1}$ in the core of the boundary layer. However, $\phi^M_{r_1}$ attains small values, and the overall effect on $\boldsymbol{\phi}_{\boldsymbol{r}_1}$ is small. Note the presence of rare (low probability) but very strong positive and negative fluxes of $\phi^F_{r_1}$ at $Y = 7L_0$. Similar behaviour has been observed for the PDFs of fluxes in homogeneous isotropic turbulence, see figure 3 in Yasuda & Vassilicos (2018) and also Ishihara, Gotoh & Kaneda (2009) and Aoyama *et al.* (2005), but in this case the time average is negative (standard forward cascade). Therefore the presence of turbulent spots in a transitional flow modifies the average picture, even though the results are spanwise-averaged and the localised spot effect is diluted; this indicates that it must be quite strong. The rare positive and negative events are still there, and it is not clear how the two forms of intermittency, one due to small-scale structures present in turbulent flows and the other due to transition, interact. This motivates a more careful analysis of interscale fluxes, for example one in which the fluxes are conditioned on the flow state (laminar or turbulent) at points x_i^+ and x_i^-. Such conditional analysis has been performed by Yao *et al.* (2020) for the second-order structure functions and can be extended to interscale fluxes as well; we leave this for future work.

https://doi.org/10.1017/jfm.2022.285 Published online by Cambridge University Press

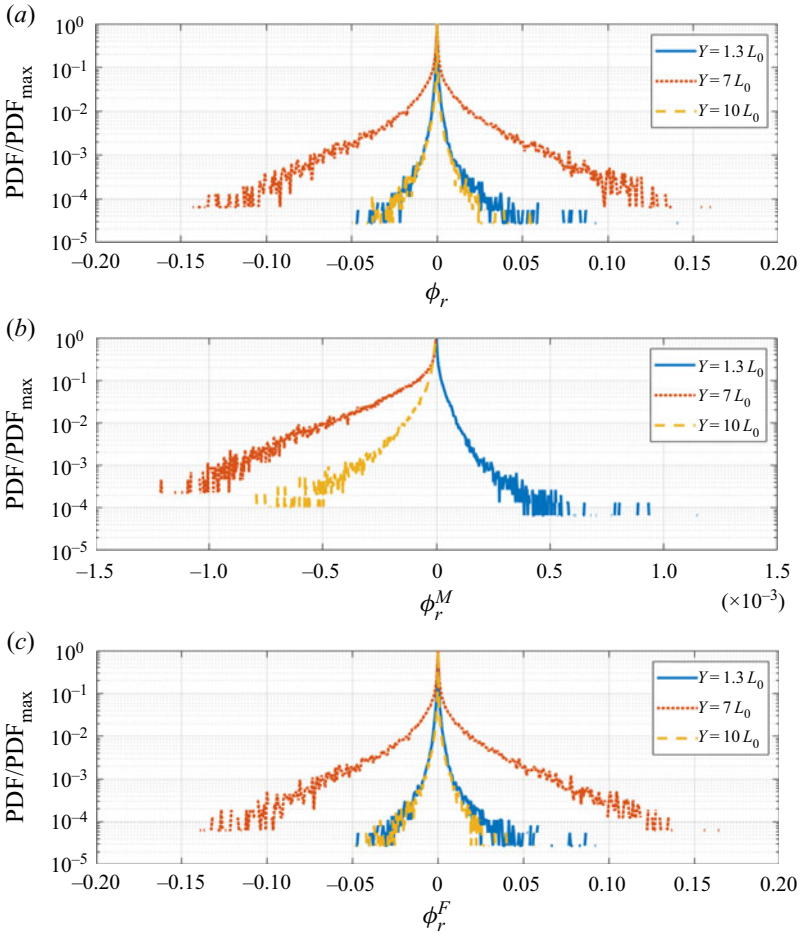


Figure 17. The PDFs of $\boldsymbol{\phi}_{\boldsymbol{r}_1}$ (a) with the mean (b) and fluctuating (c) components at $TR1$ location for $(r_1 = 50L_0, r_2 = 0.r_3 = 8L_0)$.

9. Conclusions

We apply the KHMH equation to analyse the interscale energy flux in a flat-plate boundary layer undergoing bypass transition due to forcing from free-stream turbulence. Energy from the mean flow is injected at a particular spanwise length scale and wall-normal position, both of which are determined by the interaction between the external forcing and the mean shear (linear receptivity process) that takes place in the early development of the boundary layer. This process sets the scene for the subsequent development of the interscale energy transfer and is absent in the fully developed turbulent flows that have been examined so far in the literature. From this production peak, energy fluxes radiate to different directions in physical and scale spaces. Two- and three-dimensional flux maps in the transitional regime show a very strong inverse cascade near the wall (i.e. energy flows from small to large scales) in the streamwise direction. Analysis of the constituent components of the total flux indicates that the inverse cascade is due to the nonlinear interactions between velocity fluctuations. Other components, such as that due to mean flow inhomogeneity, are non-negligible, but are not strong enough to affect the flux direction. As the transition process approaches completion, the maps morph to those

https://doi.org/10.1017/jfm.2022.285 Published online by Cambridge University Press

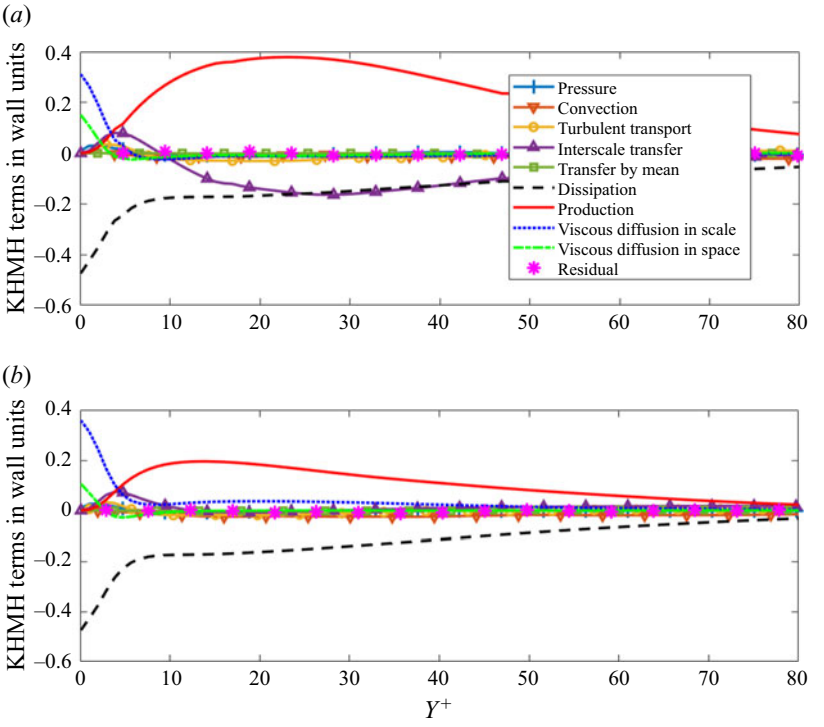


Figure 18. Budgets of the KHMH equation at location *TR*2 for $(r_3, r_1) = (0L_0, 75L_0)$ (*a*) and $(r_3, r_1) = (8L_0, 75L_0)$ (*b*).

encountered in other fully developed turbulent flows, such as channel flow, where there is weak inverse cascade in the streamwise direction, and then the flux vectors bend towards small scales.

Superposition of the instantaneous flux vectors with the corresponding flow fields relates the cascade process to the growth of turbulent structures in the streamwise direction, a unique feature of transitional flows. The sign of the time- and spanwise-average flux is positive across the boundary layer thickness and this is related to predominantly accelerating events that lead to the elongation of vortex structures within a spot, and consequently to the spot itself. These events are absent in fully developed flows. The PDF of the flux is asymmetric and skewed towards positive values. However, strong but rare forward and inverse cascade events are present, as in homogeneous isotropic turbulence.

The present results have painted a picture of interscale transfer in transitional flows that deviates significantly from that of fully developed, wall-bounded, turbulent flows. In the current work, the spanwise averaging dilutes the transfer process within nascent and developing spots, as a large proportion of the flow remains laminar in the early stages of transition. More in-depth investigations using conditional averaging, an operation that naturally accounts for intermittency effects due to transition, are certainly warranted. Such investigations will elucidate the contributions to the average interscale transfer arising from different events, i.e. when the points x_i^+ and x_i^- are both located in laminar or turbulent patches, or one is placed in a laminar and the other in a turbulent region. This will allow one to investigate the role of the laminar–turbulent interface in the cascade process.

Funding. H.Y. acknowledges financial support from the Department of Aeronautics, Imperial College London and the Imperial College-CSC scholarship. The authors also wish to acknowledge the UK Turbulence

https://doi.org/10.1017/jfm.2022.285 Published online by Cambridge University Press

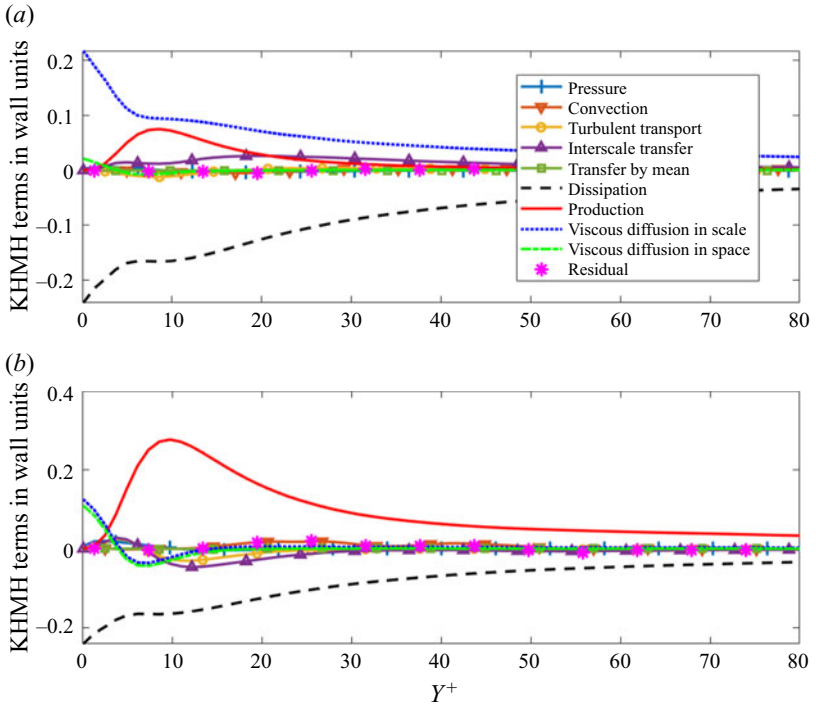


Figure 19. Budgets of the KHMH equation at the fully turbulent region (*TU*) for $(r_3, r_1) = (0.1L_0, 0L_0)$ (*a*) and $(r_3, r_1) = (18L_0, 0L_0)$ (*b*).

Consortium (UKTC) for providing access to the ARCHER high-performance computing facility through EPSRC grant EP/R029326/1.

Declaration of interests. The authors report no conflict of interest.

Author ORCIDs.
J.-P. Mollicone https://orcid.org/0000-0002-8989-4762;
G. Papadakis https://orcid.org/0000-0003-0594-3107.

Appendix

The budgets for the KHMH equation at two locations, *TR*2 and *TU*, are shown in figures 18 and 19, respectively. Two separation pairs are considered for each location, and all terms are plotted against the wall-normal direction. At small separations, the residual is less than 1 % of maximum production. At large separations, it is less than 4–5 %. Similar results have been found for other streamwise locations and separations.

References

Alves Portela, F., Papadakis, G. & Vassilicos, J.C. 2017 The turbulence cascade in the near wake of a square prism. *J. Fluid Mech.* **825**, 315–352.

Alves Portela, F., Papadakis, G. & Vassilicos, J.C. 2020 The role of coherent structures and inhomogeneity in near-field interscale turbulent energy transfers. *J. Fluid Mech.* **896**, A16.

Andersson, P., Brandt, L., Bottaro, A. & Henningson, D.S. 2001 On the breakdown of boundary layer streaks. *J. Fluid Mech.* **428**, 29–60.

https://doi.org/10.1017/jfm.2022.285 Published online by Cambridge University Press

ANTHONY, R.J., JONES, T.V. & LAGRAFF, J.E. 2005 High frequency surface heat flux imaging of bypass transition. *Trans. ASME J. Turbomach.* **127** (2), 241–250.

ANTONIA, R.A., OULD-ROUIS, M., ANSELMET, F. & ZHU, Y. 1997 Analogy between predictions of Kolmogorov and Yaglom. *J. Fluid Mech.* **332**, 395–409.

ANTONIA, R.A., ZHOU, T., DANAILA, L. & ANSELMET, F. 2000 Streamwise inhomogeneity of decaying grid turbulence. *Phys. Fluids* **12** (11), 3086–3089.

AOYAMA, T., ISHIHARA, T., KANEDA, Y., YOKOKAWA, M., ITAKURA, K. & UNO, A. 2005 Statistics of energy transfer in high-resolution direct numerical simulation of turbulence in a periodic box. *J. Phys. Soc. Japan* **74** (12), 3202–3212.

CANTWELL, B., COLES, D. & DIMOTAKIS, P. 1978 Structure and entrainment in the plane of symmetry of a turbulent spot. *J. Fluid Mech.* **87** (4), 641–672.

CIMARELLI, A. & DE ANGELIS, E. 2012 Anisotropic dynamics and sub-grid energy transfer in wall-turbulence. *Phys. Fluids* **24**, 015102.

CIMARELLI, A., DE ANGELIS, E. & CASCIOLA, C.M. 2013 Paths of energy in turbulent channel flows. *J. Fluid Mech.* **715**, 436–451.

CIMARELLI, A., DE ANGELIS, E., JIMENEZ, J. & CASCIOLA, C.M. 2016 Cascades and wall-normal fluxes in turbulent channel flows. *J. Fluid Mech.* **796**, 417–436.

CIMARELLI, A., DE ANGELIS, E., SCHLATTER, P., BRETHOUWER, G., TALAMELLI, A. & CASCIOLA, C.M. 2015 Sources and fluxes of scale energy in the overlap layer of wall turbulence. *J. Fluid Mech.* **771**, 407–423.

CIMARELLI, A., MOLLICONE, J.-P., VAN REEUWIJK, M. & DE ANGELIS, E. 2021 Spatially evolving cascades in temporal planar jets. *J. Fluid Mech.* **910**, A19.

DANAILA, L., ANSELMET, F. & ZHOU, T. 2004 Turbulent energy scale-budget equations for nearly homogeneous sheared turbulence. *Flow Turbul. Combust.* **72**, 287–310.

DANAILA, L., ANSELMET, F., ZHOU, T. & ANTONIA, R.A. 2001 Turbulent energy scale budget equations in a fully developed channel flow. *J. Fluid Mech.* **430**, 87–109.

DANAILA, L., KRAWCZYNSKI, J.F., THIESSET, F. & RENOU, B. 2012 Yaglom-like equation in axisymmetric anisotropic turbulence. *Physica* D **241** (3), 216–223.

DAVIDSON, P.A. & PEARSON, B.R. 2005 Identifying turbulent energy distributions in real, rather than Fourier, space. *Phys. Rev. Lett.* **95** (21), 214501.

DAVIDSON, P.A. 2015 *Turbulence: An Introduction for Scientists and Engineers*. Oxford University Press.

DUBRULLE, B. 2019 Beyond Kolmogorov cascades. *J. Fluid Mech.* **867**, P1.

DUCHON, J. & ROBERT, R. 2000 Inertial energy dissipation for weak solutions of incompressible Euler and Navier–Stokes equations. *Nonlinearity* **13** (1), 249–255.

DURBIN, P.A. 2017 Perspectives on the phenomenology and modeling of boundary layer transition. *Flow Turbul. Combust.* **99** (1), 1–23.

EMMONS, H.W. 1951 The laminar-turbulent transition in a boundary layer-part I. *J. Aeronaut. Sci.* **18** (7), 490–498.

GATTI, D., CHIARINI, A., CIMARELLI, A. & QUADRIO, M. 2020 Structure function tensor equations in inhomogeneous turbulence. *J. Fluid Mech.* **898**, A5.

HILL, R.J. 2002 Exact second-order structure-function relationships. *J. Fluid Mech.* **468**, 317–326.

HUNT, J.C.R. & DURBIN, P.A. 1999 Perturbed vortical layers and shear sheltering. *Fluid Dyn. Res.* **24** (6), 375–404.

ISHIHARA, T., GOTOH, T. & KANEDA, Y. 2009 Study of high Reynolds number isotropic turbulence by direct numerical simulation. *Annu. Rev. Fluid Mech.* **41** (1), 165–180.

JACOBS, R.G. & DURBIN, P.A. 2001 Simulations of bypass transition. *J. Fluid Mech.* **428**, 185–212.

DE KÁRMÁN, T. & HOWARTH, L. 1938 On the statistical theory of isotropic turbulence. *Proc. R. Soc. Lond.* A **164** (917), 192–215.

KENDALL, J.M. 1991 Studies on laminar boundary-layer receptivity to free-stream turbulence near a leading edge. In *Boundary Layer Stability and Transition to Turbulence*, pp. 23–30. ASME.

KLEBANOFF, P.S. 1971 Effect of free-stream turbulence on a laminar boundary layer. In *Bulletin of the American Physical Society*, vol. 16, p. 1323.

KNUTSEN, A.N., BAJ, P., LAWSON, J.M., BODENSCHATZ, E., DAWSON, J.R. & WORTH, N.A. 2020 The inter-scale energy budget in a von Kármán mixing flow. *J. Fluid Mech.* **895**, A11.

KOLMOGOROV, A.N. 1941 Dissipation of energy in the locally isotropic turbulence. *Dokl. Akad. Nauk SSSR* **32**, 16–18.

MARATI, N., CASCIOLA, C.M. & PIVA, R. 2004 Energy cascade and spatial fluxes in wall turbulence. *J. Fluid Mech.* **521**, 191–215.

MARXEN, O. & ZAKI, T.A. 2019 Turbulence in intermittent transitional boundary layers and in turbulence spots. *J. Fluid Mech.* **860**, 350–383.

https://doi.org/10.1017/jfm.2022.285 Published online by Cambridge University Press

MOLLICONE, J.-P., BATTISTA, F., GUALTIERI, P. & CASCIOLA, C.M. 2018 Turbulence dynamics in separated flows: the generalised Kolmogorov equation for inhomogeneous anisotropic conditions. *J. Fluid Mech.* **841**, 1012–1039.

MONIN, A.S. & YAGLOM, A.M. 1975 *Statistical Fluid Mechanics: Mechanics of Turbulence*. MIT.

MORKOVIN, M.V. 1969 On the many faces of transition. In *Viscous Drag Reduction*, pp. 1–31. Springer.

NOLAN, K.P. & ZAKI, T.A. 2013 Conditional sampling of transitional boundary layers in pressure gradients. *J. Fluid Mech.* **728**, 306–339.

PARK, G.I., WALLACE, J.M., WU, X. & MOIN, P. 2012 Boundary layer turbulence in transitional and developed states. *Phys. Fluids* **24** (3), 035105.

PERRY, A.E., LIM, T.T. & TEH, E.W. 1981 A visual study of turbulent spots. *J. Fluid Mech.* **104**, 387–405.

POPE, S.B. 2000 *Turbulent Flows*. Cambridge University Press.

ROACH, P.E. 1990 The influence of a turbulent free-stream on zero pressure gradient transitional boundary layer development: Part 1. Test cases T3A and T3B. In *ERCOFTAC Workshop, Lausanne, 1990*. Cambridge University Press.

SAIKRISHNAN, N., DE ANGELIS, E., LONGMIRE, E.K., MARUSIC, I., CASCIOLA, C.M. & PIVA, R. 2012 Reynolds number effects on scale energy balance in wall turbulence. *Phys. Fluids* **24** (1), 015101.

SINGER, B.A. 1996 Characteristics of a young turbulent spot. *Phys. Fluids* **8** (2), 509–521.

SPALART, P.R. 1988 Direct simulation of a turbulent boundary layer up to $R_\theta = 1410$. *J. Fluid Mech.* **187**, 61–98.

TOWNSEND, A.A. 1976 *The Structure of Turbulent Shear Flow*, 2nd edn. Cambridge University Press.

VAUGHAN, N.J. & ZAKI, T.A. 2011 Stability of zero-pressure-gradient boundary layer distorted by unsteady Klebanoff streaks. *J. Fluid Mech.* **681**, 116–153.

WANG, Y., CHOI, K.-S., GASTER, M., ATKIN, C., BORODULIN, V. & KACHANOV, Y. 2021 Early development of artificially initiated turbulent spots. *J. Fluid Mech.* **916**, A1.

WU, X., MOIN, P., WALLACE, J.M., SKARDA, J., LOZANO-DURÁN, A. & HICKEY, J.-P. 2017 Transitional–turbulent spots and turbulent–turbulent spots in boundary layers. *Proc. Natl Acad. Sci. USA* **114** (27), E5292–E5299.

WYGNANSKI, I., SOKOLOV, M. & FRIEDMAN, D. 1976 On a turbulent 'spot' in a laminar boundary layer. *J. Fluid Mech.* **78** (4), 785–819.

XIAO, D. & PAPADAKIS, G. 2019 Nonlinear optimal control of transition due to a pair of vortical perturbations using a receding horizon approach. *J. Fluid Mech.* **861**, 524–555.

YAO, H., ALVES-PORTELA, F. & PAPADAKIS, G. 2020 Evolution of conditionally averaged second-order structure functions in a transitional boundary layer. *Phys. Rev. Fluids* **5**, 093902.

YASUDA, T. & VASSILICOS, J.C. 2018 Spatio-temporal intermittency of the turbulent energy cascade. *J. Fluid Mech.* **853**, 235–252.

ZAKI, T.A. & SAHA, S. 2009 On shear sheltering and the structure of vortical modes in single-and two-fluid boundary layers. *J. Fluid Mech.* **626**, 111–147.

https://doi.org/10.1017/jfm.2022.285 Published online by Cambridge University Press